Materials Advances

REVIEW

View Article Online
View Journal | View Issue

Check for updates

Cite this: *Mater. Adv.*, 2022, 3, 3389

Received 18th February 2022,
Accepted 21st March 2022

DOI: 10.1039/d2ma00191h

rsc.li/materials-advances

2D material based heterostructures for solar light driven photocatalytic H_2 production

Yingying Wang, Zhu Ding, Nayab Arif, Wei-Chao Jiang* and Yu-Jia Zeng *

Photocatalytic H_2 production using solar energy has long been considered as a promising solution for renewable energy production to solve energy crisis and environmental issues. 2D materials with unique layered structures and electronic properties have led to considerable breakthroughs in energy fields. By constructing heterostructures to facilitate solar light absorption and charge transfer and separation, the photocatalytic activity of 2D materials can be highly boosted. In this review, we summarize recent progress in 2D material based heterostructures for solar light driven photocatalytic H_2 production, including black phosphorus (BP), g-C_3N_4 (CN), transition metal dichalcogenides (TMDs), layered double hydroxides (LDHs), MXenes, and other emerging 2D materials. We provide a fundamental understanding of the functions of various heterojunctions due to their enhanced photocatalytic activity. The band alignments of different heterojunctions with enhanced visible light absorption and improved charge transfer in terms of water splitting reaction are specially discussed. Finally, the existing challenges and prospects of the practical application of 2D material-based heterostructures in photocatalytic H_2 production are presented.

1 Introduction

Since solar energy is limitless, free and clean, it has become the key among renewable energy resources (biomass, wind, geothermal, marine, *etc.*) to alleviate the energy crisis and environmental issues.[1,2] Meanwhile, as an abundant element on earth, hydrogen is also the most promising energy carrier, which releases only water after usage and results in truly zero emission. Owing to its cleanliness, plentiful quantity, high-energy efficiency, storability, and easy-transportation, hydrogen plays a crucial role in driving modern energy systems for the sustainable development of humans. Thus, the conversion of solar energy into usable and storable hydrogen in both an economically and environmentally friendly way is the most desirable solution to the energy crisis issue.[3,4] The decomposition of water into hydrogen and oxygen using titania photoanodes was first reported by Honda and Fujishima in 1972;[5] since then, photocatalytic water splitting using solar energy in the presence of semiconductor photocatalysts has been studied as the potential route for H_2 production.[6,7] Afterwards, a number of materials (*e.g.*, ZnO, Fe_2O_3, WO_3, $BiVO_4$, CdSe) were developed successively with acceptable photocatalytic performance.[8–10] However, further practical applications of traditional semiconductor photocatalysts have been restricted by their low solar-to-hydrogen (STH) conversion efficiency (approximately 1%), which is due to either their large band gap or the rapid recombination of photogenerated electron–hole pairs.[11]

During the past decade, various strategies have been implemented to achieve a high efficiency of photocatalytic water splitting, including optimizing the available photocatalysts and exploring new types of photocatalysts and heterostructures.[12,13] Two-dimensional (2D) materials with van der Waals (vdW) stacking of layers of atoms have been well recognized as rising stars following the successful isolation of graphene in 2004.[14] 2D materials include 2D allotropes of various elements (*e.g.*, graphene, borophene, silicene, phosphorene and germanene) or compounds (*e.g.*, h-BN, g-C_3N_4 (CN), transition metal dichalcogenides (TMDs), MXenes, layered double hydroxides (LDHs)), whose family is still growing.[15–18] These 2D materials with unique structural and electronic properties result in extensive breakthroughs in the catalysis and energy conversion fields.[19–21] It has been found that 2D semiconductors which have large specific surface areas with abundant surface-active sites could be promising photocatalysts providing superior electron mobility and short diffusion distance for efficient charge separation.[22–24] Moreover, the planar structure of 2D materials with weak vdW force and dangling-bond-free surfaces allows the facile formation of heterostructures, which are integrated with not only 2D materials but also materials of different dimensionalities. The construction of heterostructures offers unique properties and promotes photocatalytic activity resulting from the synergies of their individual components.[25–27] Various heterostructures of 2D materials have

Key Laboratory of Optoelectronic Devices and Systems of Ministry of Education and Guangdong Province, College of Physics and Optoelectronic Engineering, Shenzhen University, Shenzhen 518052, Guangdong, China.
E-mail: jiang.wei.chao@szu.edu.cn, yjzeng@szu.edu.cn

been synthesized successfully with optimized kinetics and energetics for photocatalytic water splitting.[26,28,29] Previous reviews have been focused on individual 2D materials, such as BP based heterostructures,[30–32] CN based heterostructures,[33,34] and TMD based heterostructures,[35–38] or focused on photocatalysis for environmental remediation,[38,39] or on DFT calculation results.[40] As the family of 2D materials is extending rapidly, an updated review of all-inclusive 2D material based heterostructures for photocatalytic H_2 production is needed, in particular for their fundamental mechanisms.

Herein, we summarize recent advances of well functioned heterostructures based on various 2D materials, including BP, CN, TMDs, MXenes, and LDHs, and their applications in photocatalytic H_2 production. Various 2D material-based heterojunctions are systematically discussed, such as type-I, type-II, Z-scheme, S-scheme and Schottky junctions. The band alignments in heterojunctions successfully enhance visible light absorption and suppress the recombination of photogenerated electron–hole pairs. Construction of vdW heterostructures can provide abundant surface-active sites for photocatalytic reactions. Moreover, the intimate interfacial contact between two components can also improve the charge transfer and separation of photogenerated electron–hole pairs. Owing to the synergy of components in the heterostructure, the efficiency of photocatalytic H_2 production is highly improved. Many innovative studies on efficient visible light driven photocatalysts achieving remarkable H_2 production results are particularly highlighted. This review provides comprehensive and critical information for developing vdW based heterostructures with excellent photocatalytic properties. Finally, our prospects on the explorations of vdW heterostructures in the field of renewable energy production are also presented.

2 Introduction to van der Waals (vdW) heterostructures

The family of 2D materials consisting of different elements is expanding dramatically, which is highlighted in Fig. 1. In addition to graphene, a series of layered materials were continuously exfoliated into their 2D forms, including graphene-like hexagonal boron nitride (h-BN),[41,42] graphitic carbon nitride (CN),[43–45] transition metal dichalcogenides (TMDs),[46,47] group-III monochalcogenides,[48–50] and layered double hydroxides (LDHs).[51–54] Emerging members such as black phosphorus (BP),[55–57] MXenes,[24,58,59] silicene,[60,61] metal–organic frameworks (MOFs),[62–64] and polymers[65–67] were further flourished in the energy-related areas. When 2D materials are applied in photocatalytic/photoelectrochemical water splitting, the photons are absorbed by photocatalysts and electron–hole pairs are generated for the subsequent redox reactions. The severe recombination of electron–hole pairs largely suppresses the solar-to-hydrogen conversion efficiency.[68] By constructing heterostructures, the charge separation and transfer are highly improved and the recombination of electron–hole pairs are effectively prevented.[69]

Avoiding direct chemical bonding between different layers and constraints of crystal lattice matching, 2D materials bring more possibilities for heterostructures with mixed dimensions. For example, 0D nanoparticles and quantum dots (QDs),[70] 1D nanowires and nanorods,[71] and 1.5D nanosheets/nanoflakes (non-vdW structures but 2D morphologies)[29] can be constructed with vdW heterostructures as shown in Fig. 2. A vdW hybrid (vdWH) not only combines the properties of the original component materials but also exhibits novel physicochemical properties and unique functions. For example, the MoS_2/WSe_2 heterostructure was reported to achieve ultrafast charge dynamics within a timescale of 100 fs.[72,73] The ultrafast transfer of photo-excited electrons was also found in the BP/InSe heterostructure.[74] The band alignment of the g-GaN/$Mg(OH)_2$ vdWH boosted the oxidation and reduction reactions for water splitting. And the potential drop across the interface of the heterostructure could lead to a large built-in electric field which promotes charge separation.[75] The electronic properties and band gap structure of the ZnO/GaN vdWH can be tuned using external biaxial strain for realizing high photocatalytic activity.[76] Therefore, vdW heterostructures could be promising photocatalysts or co-catalysts for photocatalytic/photoelectrochemical water splitting.

Depending on the band structures of 2D material-based heterostructures, there are mainly four types of heterojunctions (straddling alignment (type-I), staggered alignment (type-II), Z-scheme, and S-scheme heterojunctions), as illustrated in Fig. 3. In a type I heterojunction, the VB and CB of semiconductor 1 are lower and higher than those of semiconductor 2, respectively. Therefore, the photogenerated electrons and holes from

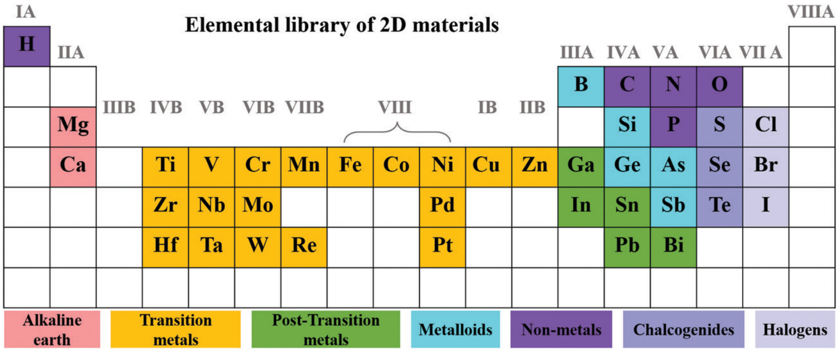

Fig. 1 Element distribution of 2D materials in the periodic table.

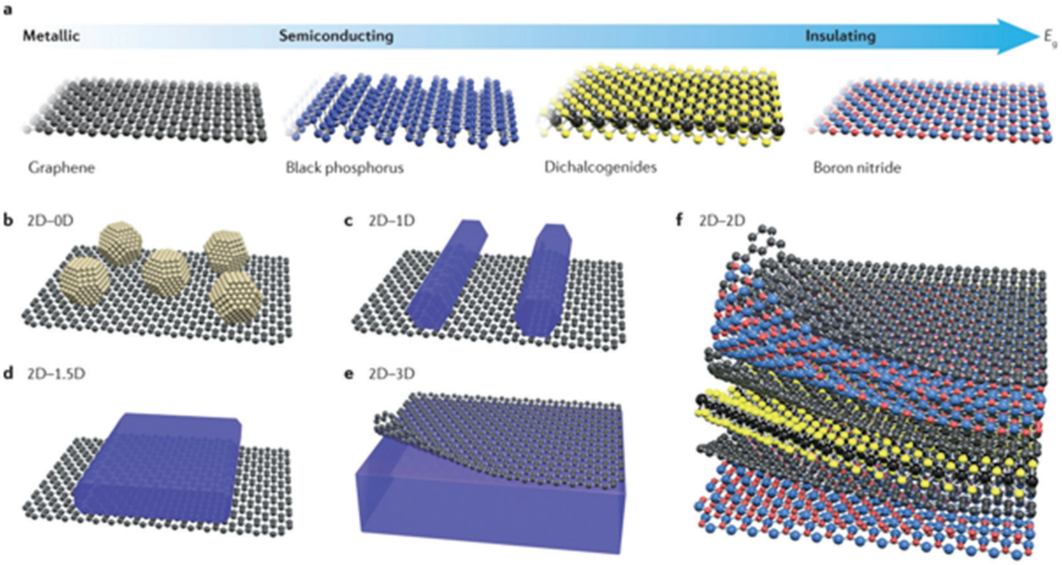

Fig. 2 (a) Frontiers of some 2D materials and typical vdWHs: (b) 2D–0D, (c) 2D–1D, (d) 2D–1.5D, (e) 2D–3D, and (f) 2D–2D. Reprinted with permission.[77] Copyright 2017 Nature.

semiconductor 1 can migrate to the CB and VB of semiconductor 2, respectively. However, the electrons in the CB of semiconductor 2 still easily recombine with holes in the VB of semiconductor 2, resulting in limited improvement in charge carrier separation. It is

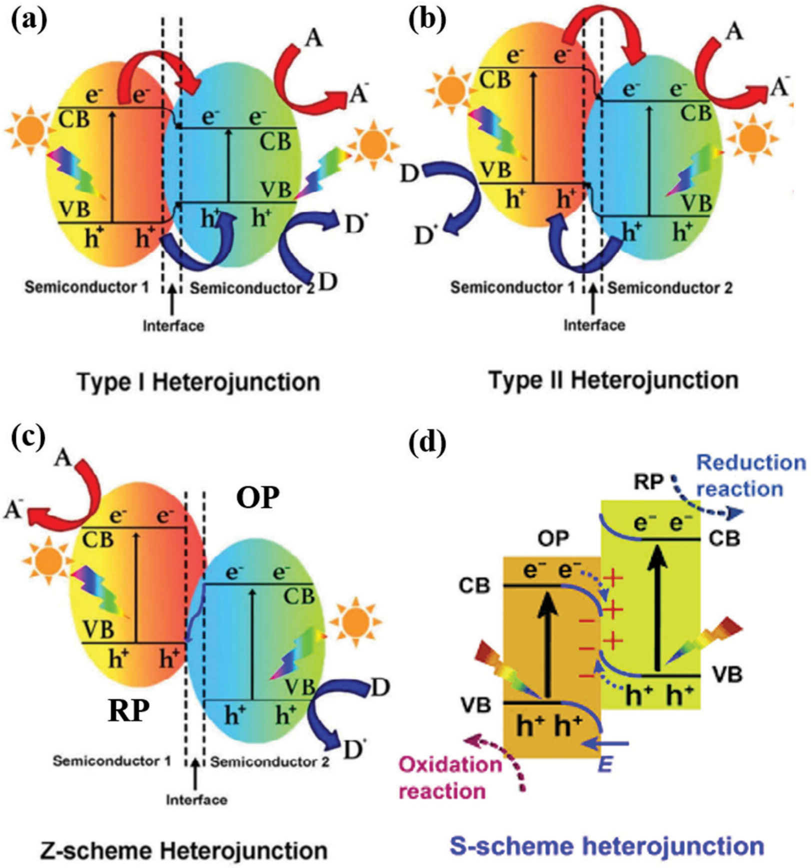

Fig. 3 Band structures of various types of heterojunctions: (a) type I heterojunction, (b) type II heterojunction, and (c) Z-scheme heterojunction. Reproduced with permission.[90] Copyright 2019 Elsevier. (d) S-scheme heterojunction. Reprinted with permission.[88] Copyright 2019 Elsevier. A, D and E, F represent the electron acceptor, electron donor and Fermi level, respectively.

worth noting that a work function difference between two semiconductor photocatalysts is the pre-requisite for inducing charge redistribution and the formation of an internal electric field, which significantly affect the photogenerated charge carrier separation and transfer processes. In a type II heterojunction, both the CB and VB of semiconductor 2 are lower than those of semiconductor 1, forming a stable heterostructure. The photoinduced electrons and holes can migrate to the CB of semiconductor 2 and the VB of semiconductor 1 and the steps in the CB and VB go in the same direction. Importantly, the difference of chemical potential between semiconductors 1 and 2 causes band bending at the interface of the junction. The band bending induces a built-in field, which drives the photogenerated electrons and holes to move in opposite directions, leading to a spatial separation of the electrons and holes on the different sides of the heterojunction. Therefore, the efficient spatial separation of charge carriers and a prolonged electron lifetime are achieved. Despite the competency of the heterojunction-type of 2D-materials in facilitating charge separation, the redox ability of the photocatalytic system is weakened due to the migration of electrons and holes to the more electropositive CB and electronegative VB, respectively, ascribed to the nature of charge transfer, as shown in Fig. 3b. In the type II heterojunction system, electrons and holes accumulate in the less negative CB and the more positive VB of the photocatalyst, respectively, resulting in weakened reduction and oxidation potentials.

Inspired by natural photosynthesis, Bard *et al.*[78] proposed a Z-scheme system in 1979 to optimize the redox potentials of heterojunctions. As compared to a type-II heterojunction, a Z-scheme photocatalyst has the same band structure configuration and a distinctly different charge carrier transfer mode. However, the Z-scheme heterojunction can maintain the redox ability of photogenerated charge carriers after charge transfer. By adjusting electron mediators, the charge transfer path changes and the type-II heterojunction can be transformed to the Z-scheme system.[79–81] The conventional Z-scheme photocatalytic system consists of an H_2 production photocatalyst (HPP) or reduction photocatalyst (RP), A; an O_2 production photocatalyst (OPP) or oxidation photocatalyst (OP), B; and redox mediators.[82] The electrons in the CB of the OP combine with the holes in the VB of the RP through an electron mediator, facilitating the photogenerated electron–hole pairs on the OP and RP but maintaining their reduction and oxidation potentials. But the Z-scheme system still has some problems, such as redox mediator reverse (back) reactions, light-shielding effects, and low charge transfer by ion diffusion. Later, Tada *et al.* proposed all-solid-state Z-scheme photocatalytic systems using solid conductors as electron mediators in 2006,[83] such as noble-metal particles[84] and reduced graphene oxide (RGO).[85] The selection of an appropriate electron conductor is crucial because it can not only efficiently transfer the photogenerated charge carriers but also effectively improve the stability of the photocatalysts.

The direct Z-scheme photocatalytic system includes only an HPP and an OPP without electron mediators as shown in Fig. 3c. The photogenerated electrons in the lower-level CB of semiconductor 2 can directly recombine with the photoinduced holes in the higher-level VB of semiconductor 1. The higher CB and VB of semiconductor 1 have lower work functions, but higher Fermi levels than semiconductor 2. When semiconductors 1 and 2 are in contact, free electrons keep moving from semiconductor 1 to semiconductor 2 until they reach an equilibrated Fermi level with negative and positive charges at interfaces. Furthermore, a built-in electric field is formed and band edge bending occurs. This Z-scheme system can effectively inhibit the backward reaction of H_2 and O_2 into H_2O.[86,87] It is worth noting that the induced electric field can also suppress the recombination between the photogenerated electrons of semiconductors in the Z-scheme and also maintained the oxidation and reduction reactions in a timely manner.

A step-scheme (S-scheme) heterojunction is similar to a type-II heterojunction with an OP and an RP but with a completely different charge-transfer route as shown in Fig. 3d.[88,89] The RP has higher CB and VB positions and a higher Fermi level with respect to the OP. Thus, the electrons spontaneously transfer from the RP to OP until the Fermi level equilibrium is reached, resulting in an internal electric field (IEF). The charge-transfer route from the low CB of the OP to the high CB of the RP resembles a "step" in the S-scheme system. The alignment of the Fermi energies of the RP and OP to the same level leads to upward and downward shifts in the Fermi levels of the RP and OP, respectively. Therefore, the S-scheme system typically has the features of the built-in IEF and the band bending effect. The photoexcited electron–hole pairs are spatially separated in the S-scheme system due to the IEF, located in the CB of the RP and the VB of the OP, respectively. On the other side, the unused electrons in the CB of the OP and the holes of the VB of the RP recombine and disappear. Thus, the S-scheme heterostructure reserves the photogenerated electron–hole pairs from both the RP and OP, resulting in a powerful redox ability for photocatalytic water splitting.

Both Z-scheme and S-scheme photocatalysts are composed of two tandem structured photosystems that can meet the requirements of higher wavelength absorption and wideband energy gaps between the conduction and valence bands. However, the two-photon excitation mechanism reduces half of the efficiency of the system. Notably, the coupling of two semiconductors in which semiconductor 1 has a higher Fermi level will induce a negatively charged interface, which eventually leads to the formation of a direct Z-scheme system. Conversely, when semiconductor 1 has a lower Fermi level, a type-II heterojunction will be formed. The quasi-continuous energy state at the solid–solid interface of the photocatalyst system can bestow an internal electric field for vectorial electron flow with low resistance.

Other heterostructures such as p–n junctions combining p-type and n-type semiconductors and Schottky or ohmic junctions coupling semiconductors and metal-like materials can also promote charge transfer and separation as well as photocatalytic performance. The specific function and working mechanism of these heterojunctions based on various 2D materials for photocatalytic H_2 generation are illustrated in Section 3.

3 Various 2D material based heterostructures

3.1 Black phosphorus-based heterostructures

Black phosphorus (BP) has received enormous research interest in recent years owing to its anisotropic 2D layered structure, tuneable gap energy (0.3–2.0 eV), and high charge carrier mobility.[91–93] The crystal structure of monolayer BP consists of a repeated puckered honeycomb structure along the armchair direction as shown in Fig. 4a. The vdW forces hold interactions between layers along the crystallographic zigzag direction. Depending on the thickness or the number of layers as shown in Fig. 4b, the band gap between and the positions of the valence band maximum (VBM) and the conduction band minimum (CBM) can be adjusted. The unique structure and extraordinary electronic properties make BP a promising catalyst especially for solar light photocatalytic water splitting.[30,94] By constructing heterojunctions of BP with other materials such as TiO_2,[95] WO_3,[96] CdS,[97] and TMD materials[98,99] as shown in Fig. 4c, the excitation energy of these heterostructures can be extended to the visible light and near-infrared regions.

3.1.1 Type-I heterojunctions. When the band gap of semiconductor A covers that of semiconductor B, a straddling band alignment (type-I) is formed. The 2D/2D vdW heterojunction of CN (A) and BP (B) is usually type-I, which effectively boosts charge separation as well as the subsequent photocatalytic activity.[100–102] The hybridization of the UV-vis light response of CN and the UV-vis-NIR response of BP allows for the efficient utilization of the full spectrum of solar light. The typical 2D–2D heterostructure of CN and BP with advantageous contact and affinity facilitates charge transfer at the interface for photocatalytic reactions. Thus, the metal-free heterostructure of BP and CN optimizes the physicochemical properties of the type-I system and highly improves the kinetics of photocatalytic reactions for H_2 production.[103]

Zhu *et al.*[104] reported a BP/CN binary nanohybrid as a metal-free photocatalyst for efficient H_2 production (428.9 μmol h^{-1} g^{-1}

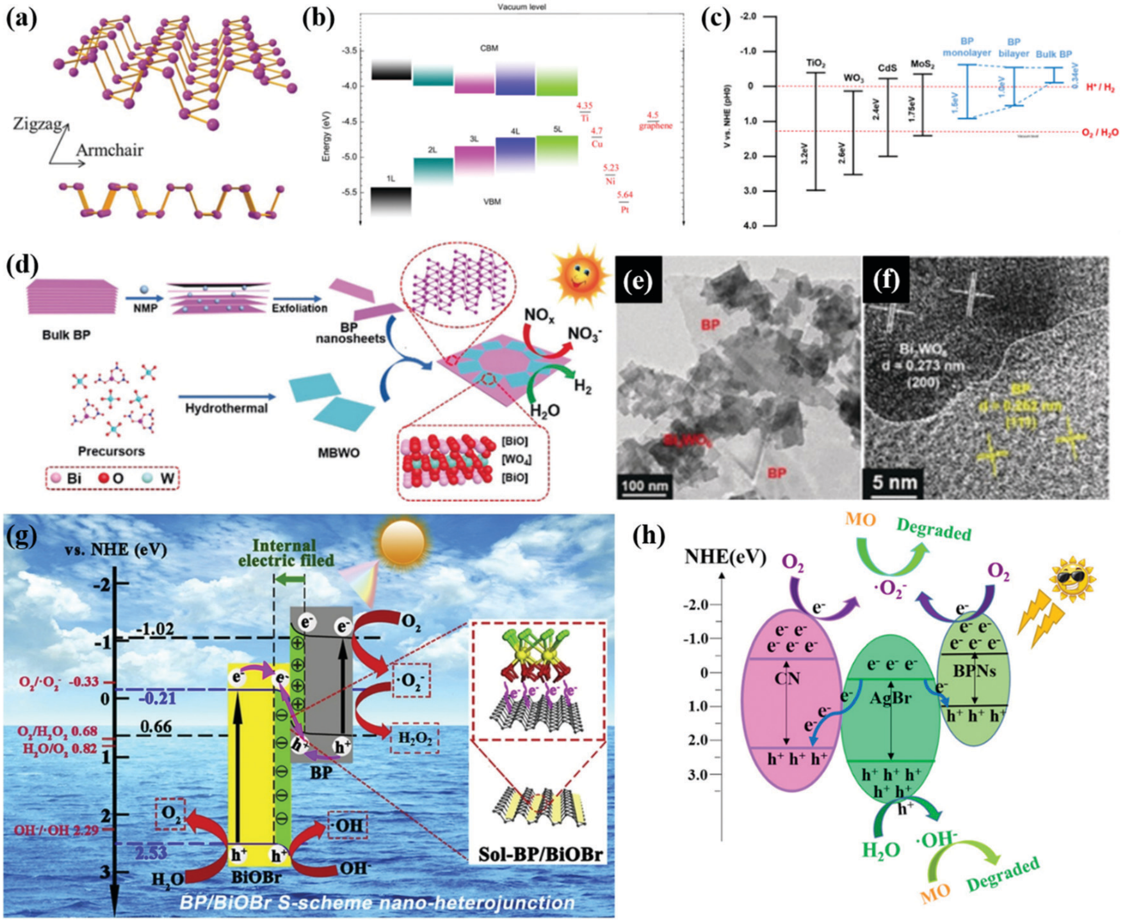

Fig. 4 (a) The top view and cross-sectional view of the atomic structure of monolayer BP. Reproduced with permission.[118] Copyright 2018, Wiley-VCH. (b) Variation of the VBM and CBM for few-layer phosphorene with the number of layers (from 1 L to 5 L) determined from HSE06 calculation. Reprinted with permission.[119] Copyright 2014, Nature. (c) Reprinted with permission.[32] Copyright 2016, MDPI. (d) Illustration of the fabrication, (e) morphology and (f) HR-TEM of the BP/Bi_2WO_6 heterojunction. Reproduced with permission.[115] Copyright 2019, Wiley-VCH. (g) S-scheme photocatalytic charge transfer and reaction mechanism between BiOBr and BP. Reproduced with permission.[116] Copyright 2020, Elsevier. (h) The proposed photocatalytic mechanism of CN/AgBr/BPN photocatalysts. Reproduced with permission.[117] Copyright 2021, Elsevier.

and 102.2 μmol h^{-1} g^{-1}) under both >420 and >780 nm light irradiation, respectively. The BP/CN nanocomposite also exhibited a promising photocatalytic H_2 evolution of 571 μmol h^{-1} g^{-1} under visible light.[105] Wen *et al.* synthesized a low-cost (0.235 Euro per gram) BP/CN heterostructure with abundant active sites leading to superior photocatalytic performance for H_2 production, 786 μmol h^{-1} g^{-1}.[106] The BP can act as an electron acceptor and provide transfer channels of electrons from the CB of CN to the CB of BP. Moreover, the p–n defect sites existing at the interface of BP and CN help in trapping electrons in the CB of BP, inhibiting the recombination of electron–hole pairs. Therefore, the heterojunction of BP and CN largely promotes the kinetics of photocatalytic redox reactions. In addition to the preferable carrier migration, the strong and intimate interface interaction of BP and CN can ensure the long-term stability of photocatalytic activity. Besides, adding transition metal phosphides as co-catalysts can further improve the photocatalytic activity of BP and CN. For example, a novel heterostructure of 2D-Ni_2P@BP and CN was found to exhibit a remarkable H_2 production rate of 858.2 μmol h^{-1} g^{-1}, which is much higher than that of Pt loaded CN owing to the rational design of the co-catalyst system and the synergetic effect among BP, Ni_2P and CN.[107] Obviously, 2D–2D heterostructures of BP and CN with type-I heterojunctions show impressive charge separation and migration as well as high photocatalytic performance.

3.1.2 Type-II heterojunctions. When both the CB and VB positions of semiconductor A are higher than those of BP, type-II heterojunctions usually form with metal oxides such as TiO_2 and WO_3, and metal-sulfides like CdS.[108] In the type-II heterojunctions, the photoexcited electrons transfer from the CB of semiconductor A to the CB of BP, while the holes migrate from the VB of BP to the VB of semiconductor A, improving the charge separation and photocatalytic reactions.[109] Chen *et al.*[110] provided an insightful investigation of the superior photocatalytic performance of the BP/$BiVO_4$ type-II heterojunction and the physicochemical mechanism behind its photocatalytic activity using first-principles calculations. The analysis of the work function, charge density difference, and Bader charge indicates that the recombination of electron–hole pairs could be inhibited by the internal electric field between the interfaces of the BP/$BiVO_4$ heterojunction. Moreover, the optical absorption coefficient of the BP/$BiVO_4$ heterostructure is found to be higher than the individual components under visible-light irradiation. Therefore, the BP/$BiVO_4$ type-II heterostructure often has a strong redox ability and exhibits high photocatalytic activity for H_2 production.

Ran *et al.*[111] for the first time achieved the application of type-II heterojunctions of phosphorene/CdS, $Zn_{0.8}Cd_{0.2}S$ and ZnS guided by density functional calculations. The excellent photocatalytic activity for H_2 production (11 192 μmol h^{-1} g^{-1}) and highly improved solar light utilization efficiency (quantum yield of 34.7% at 420 nm) were attributed to the strong electronic coupling between phosphorene and CdS and the high charge mobility of the heterostructure.

Elbanna *et al.* reported a type-II heterostructure of BP nanosheets (NS) and TiO_2 meso-crystals, which exhibited visible-NIR-driven photocatalytic activity for H_2 evolution (1.9 and 0.41 μmol h^{-1} under visible (420–1800 nm) and NIR (780–1800 nm) irradiation, respectively).[109] The type-II charge transfer at the interface of BP and TiO_2 facilitates the electron migration from BP to TiO_2. Moreover, femtosecond time-resolved diffuse reflectance spectroscopy (fs-TRDRS) and photoelectrochemical measurements not only confirmed the importance of improved charge transfer and separation but also illustrated the enhanced electron injection from the BP NS to TiO_2 by decreasing the thickness of the BP NS.

3.1.3 Z-scheme systems. Many BP-based Z-scheme systems have been prepared for photocatalytic water splitting.[112–114] Zhu *et al.*[29] designed a 2D heterostructure of BP and $BiVO_4$, allowing for a staggered alignment on the band structure and boosting the charge separation. Thus, the photogenerated electrons in the CB of BP and the photogenerated holes in the VB of $BiVO_4$ effectively accounted for the reduction and oxidation reactions, respectively. Liu *et al. in situ* constructed[113] a BP/red phosphorus (RP) hetero-phase junction photocatalyst with the same chemical composition but different crystal lattices. In addition to the virtue of band structures with a staggered alignment, the high-quality interfacial contacts between the BP and the matrix of RP directly lead to the efficient separation and transfer of photogenerated electrons and holes. Therefore, the reduction for H_2 production and the oxidation reaction for O_2 production successfully occurred in BP and RP, respectively.

Bulk BP was normally exfoliated into a few layers, assisted by NMP-intercalation as shown in Fig. 4e. By a simple hydrothermal process of precursors of Bi_2WO_6 and ultrathin BP nanosheets, Hu *et al.*[115] synthesized a Z-scheme heterojunction of BP monolayer Bi_2WO_6 (MBWO) with intimate face-to-face contact as shown in Fig. 4f and g. The photogenerated electrons in the CB of MBWO combine with the holes in the VB of BP, while electrons that remain in the CB of BP are used to produce H_2 from water splitting. The highest H_2 evolution rate of BP/MBWO can reach 21 042 μmol g^{-1}, which is more than 9 times that of pristine MBWO. In this work, the photoelectrochemical measurements and electrochemical impedance spectroscopy (EIS) spectra confirmed the excellent separation ability and efficient charge transfer of BP/MBWO.

3.1.4 S-scheme systems. BP with a higher Fermi level normally acts as a RP in a heterojunction, while BiOBr is an OP with a lower Fermi level. When BP is closely in contact with BiOBr, the electrons in BP will spontaneously transfer to BiOBr until the equilibrium of their Fermi levels is reached.[116] An IEF from BP to BiOBr was formed at the interface as shown in Fig. 4g. Driven by the IEF, the photogenerated electrons in the CB of BiOBr prefer to recombine with the holes in the VB of BP. The significant enhancements in spatial charge separation and redox capability highly boost the photocatalytic activity of BP/BiOBr.

Wang *et al.*[117] reported a AgBr/CN/BP double S-scheme heterojunction with excellent photostability and photocatalytic activity. As shown in Fig. 4h, the Fermi level of the main photocatalyst AgBr is lower than those of CN and BP, leading to transfer of electrons from CN and BP to AgBr. IEFs exist at both the CN/AgBr and AgBr/BP contact surfaces. Driven by the IEF and band bending, the photogenerated electrons migrate from the CB of AgBr to the VB of CN and BP, forming a double S-scheme which facilitates the photocatalytic reactions. The research of S-scheme heterostructures especially based on BP materials for photocatalytic water splitting is still at an early stage. An in-depth understanding of charge transfer routes and rules in S-scheme systems and further application of S-scheme heterostructures is expected. Owing to the large contact area and superior charge mobility of 2D materials including BP, more efforts should be devoted to 2D material-based S-scheme heterojunctions for photocatalytic water splitting.

3.2 CN-based heterostructures

Graphitic carbon nitride (CN) has a 2D structure of tri-*s*-triazine connected *via* tertiary amines (see Fig. 5a) with high thermal stability and chemical stability. It is identified to be one of the most promising photocatalysts for solar energy conversion owing to its appropriate electronic band structure, low cost, superior stability, facile preparation, and good compatibility with other materials.[101,120–123] To improve the STH efficiency of CN, constructing heterostructures of CN is the main strategy to enhance the light utilization and carrier mobility and the resulting photocatalytic activity.[124–126] CN-based heterostructures not only boost spatial charge separation but also allow for novel features originating from the synergistic effects between the components of the heterostructures.[127] The rational design of CN-based heterostructures can be classified into conventional type II, Z-scheme, S-scheme and other heterostructures such as Schottky and PN junctions.

3.2.1 Type II heterostructures. Pristine CN has a bandgap of 2.7 eV, with the CBM and the VBM located at approximately −1.1 and +1.6 eV (*vs.* NHE, at pH 0), respectively.[128,129] When CN is composited with an OP with a more negative CBM than that of CN, the electrons transfer from the CB of the OP component to the CB of CN, and the photogenerated electrons accumulated in the CB of CN for the reduction reaction as shown in Fig. 5b. While a RP with a more positive CBM contacts with CN, the photogenerated holes remain at the VB of CN for

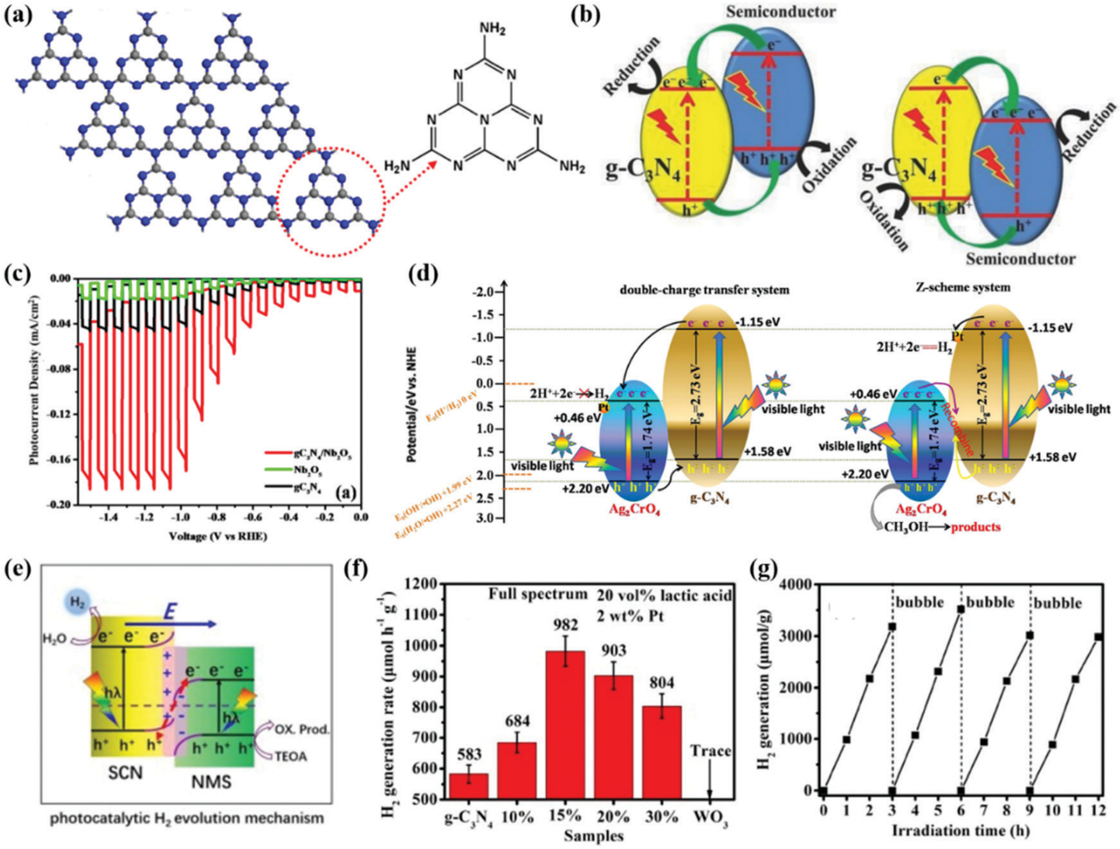

Fig. 5 (a) Tri-*s*-triazine-based two-dimensional structure of CN. Color scheme: C, gray; N, blue. Reprinted with permission.[155] Copyright 2014, American Chemical Society. (b) Charge transfer in conventional type II CN-based heterojunction systems. Reprinted with permission.[124] Copyright 2017 Wiley-VCH. (c) PEC water splitting measurements of CN, Nb_2O_5 and CN/Nb_2O_5 photoanodes. Reprinted with permission.[139] Copyright 2018 American Chemical Society. (d) Schematic representation of the charge migration and H_2 production mechanism of the Z-scheme g-CN/Ag_2CrO_4 heterostructure. Reprinted with permission.[146] Copyright 2018, Nature. (e) Proposed photocatalytic H_2 evolution mechanism over the NMS/SCN S-scheme heterojunction. Reprinted with permission.[156] Copyright 2021, Elsevier. (f) Comparison of the H_2 generation activities of the as-prepared samples. (g) Time courses of photocatalytic H_2 generation of 15%WO_3/CN. Reprinted with permission.[153] Copyright 2020 Elsevier.

oxidation reaction. CN can form type II heterojunctions with various metal oxides (TiO_2, WO_3, SnO_2, *etc.*),[130,131] metal sulfides (CdS, ZnS, MoS_2, $ZnIn_2S_4$, *etc.*),[132–134] halides (BIOI, BiOCl, AgBr, *etc.*),[135,136] and other semiconductors (Ta_3N_5, SiC, *etc.*).[137,138]

The engineered CN/Nb_2O_5 type-II heterojunction exhibited a significantly enhanced photocurrent response, which reached −0.17 mA cm^{-2}, with good stability in the photoelectrochemical (PEC) water splitting measurements as presented using red lines in Fig. 5c.[139] The Mott–Schottky (MS) analysis confirmed the negative shift of the CBM of the heterojunction between CN and Nb_2O_5 towards a lower potential of the hydrogen evolution reaction (HER). The EIS measurements further verified the efficient charge transfer derived from the suppressed recombination of photogenerated electrons and holes. Therefore, the CN/Nb_2O_5 heterojunction practically facilitates the migration of charge carriers, prolongs the lifetime of electron–hole pairs, and enhances the H_2 production from PEC water splitting. Qin *et al.*[140] reported a Ni_2P-$Cd_{0.9}Zn_{0.1}S$/CN heterostructure with a high-quantum-yield of photocatalytic H_2 production. The CN photocatalyst with a more negative CBM acts as an OP, while the $Cd_{0.9}Zn_{0.1}S$ act as an RP, forming a type-II heterojunction. The Ni_2P nanoparticles act as the active sites on $Cd_{0.9}Zn_{0.1}S$, accumulating the photoinduced electrons for reduction reaction. The Ni_2P-$Cd_{0.9}Zn_{0.1}S$/CN ternary heterostructure resulted in a high H_2 evolution rate of 2100 μmol h^{-1} g^{-1} and a corresponding apparent quantum yield (AQY) of 73.2% at 420 nm. Due to the superior photostability of CN, the photo-corrosion of $Cd_{0.9}Zn_{0.1}S$ could be alleviated, leading to a stable PEC performance for 90 h.

A semiconductor with a narrow bandgap can not only achieve a type II band alignment when composited with CN for spatial charge separation but also act as a light sensitizer for visible light absorption. Yu *et al.*[141] designed conjugated polymers, (N-annulated perylene/P3)/CN heterojunctions, with an increased light capture ability and charge separation for enhanced H_2 production under visible light. Since the lowest unoccupied molecular orbital (LUMO) and highest occupied molecular orbital (HOMO) levels of the polymers are higher than the CBM and VBM of CN, P3/CN forms a type-II heterojunction with the function of spatial charge separation. The polymer P3 with a strong electron donor unit (N-annulated perylene) has a narrow optical gap of 1.85 eV, which extends the light response to the visible and even near-infrared regions of the P3/CN heterostructure. With a broader visible-light response range and more effective charge separation, the P3/CN heterostructure exhibits a significantly increased H_2 production rate of 13.0 mmol h^{-1} g^{-1} with an AQY of 27.32% at 520 nm.

With efficient charge transfer and spatial separation of type II heterojunctions and improved light utilization, a highly enhanced photocatalytic performance for H_2 production can be obtained over CN-based heterostructures.

3.2.2 Z-scheme heterostructures. A Z-scheme heterojunction has a stronger redox ability than a type-II heterojunction. Various CN based Z-scheme heterostructures have been designed and reported for photocatalytic H_2 production.[142–145] Che *et al.*[146] reported a heterostructure of CN and Ag_2CrO_4, which exhibited 14 times higher H_2 production efficiency than bare CN under visible light. The significantly enhanced photocatalytic performance could be attributed to the direct Z-scheme charge transfer mechanism as shown in Fig. 5d. Both the CBM and VBM of Ag_2CrO_4 are more negative than those of CN. The photogenerated electrons in the CB of Ag_2CrO_4 tend to transfer to the VB of CN and combine with the holes of CN. The recombination of electron–hole pairs in Ag_2CrO_4 and CN is thus inhibited. The Pt acts as the co-catalyst and electron acceptor, which promotes water reduction reaction for H_2 production. And the photoluminescence (PL) spectra and photocurrent measurements further confirm the efficient charge separation in the CN/Ag_2CrO_4 Z-scheme heterostructure. The TiO_2/CN Z-scheme system was reported to exhibit an optimum H_2 production rate of 4128 μmol h^{-1} g^{-1} (7.7 fold that of pristine CN) under solar light irradiation.[147] The excellent photocatalytic activity could be attributed to the synergistic effects of the Z-scheme heterostructure with an extended visible light response, spatial charge separation and a maximized redox potential.

The successful employment of heterostructures for photocatalysis depends on not only band engineering but also the construction of intimate contact between the components. You *et al.*[148] constructed a Z-scheme heterostructure of CN and Bi_4NbO_8Cl with intimate interfaces realized an H_2 production rate 6.9 and 67.2 times that of bare CN and Bi_4NbO_8Cl, respectively. The PEC measurement and time-resolved photoluminescence decay (TRPLD) results clearly indicate efficient charge transfer and separation in the Z-scheme CN/Bi_4NbO_8Cl heterostructure. The electron spin resonance (ESR) spectra of CN/Bi_4NbO_8Cl further detected signals from both superoxide radicals ($^{\bullet}O_2^{\bullet-}$) and hydroxyl radicals ($^{\bullet}OH^{\bullet}$), directly verifying the Z-scheme charge transfer route. Ye *et al.*[149] also reported a Z-scheme heterostructure of $CoTiO_3$ and CN, which achieved an impressive H_2-evolution rate of 858 μmol h^{-1} g^{-1} under solar light.

Apparently, the construction of CN-based Z-scheme heterostructures facilitates charge transfer for the subsequent photocatalytic reduction and oxidation reactions. In addition to the improved solar light utilization and optimal redox potential, the H_2 production rate of these heterostructures is highly promoted under solar light.

3.2.3 S-scheme heterostructures. The built-in IEF in S-scheme systems can facilitate the separation of charge carriers and photocatalytic reactions of water splitting. Thus, CN-based S-scheme heterostructures have also been widely employed as photocatalytic systems.[150–152] For instance, Fig. 5e presents the S-scheme heterojunction of N-doped MoS_2 (NMS) and S-doped CN (SCN). According to the DFT calculation, the work function of NMS was higher than that of SCN, driving the flow of electrons from the SCN to NMS until the Fermi level equilibrium was reached. With the help of the IEF, the photoexcited electrons in the CB of SCN and holes in the VB of NMS were maintained to participate in the subsequent photocatalytic reactions. With an optimal redox potential and efficient spatial charge separation, NMS/SCN achieved a high H_2 evolution rate of 658.5 μmol g^{-1} h^{-1}, which was about 23 and 38 times higher than those of pure SCN and NMS, respectively.

By enlarging the contact area of CN with a counterpart photocatalyst, the interfacial charge transfer rate can be further enhanced. Fu *et al.*[153] designed a heterostructure of ultrathin WO_3 and CN nanosheets of 2.5–3.5 nm (equivalent to 5–8 atomic or molecular layer thickness). Fig. 5f presents the photocatalytic performance of the WO_3/CN heterostructure and reference samples. Apparently, the 15% WO_3/CN photocatalyst sample exhibits the highest H_2-production rate of 982 μmol h^{-1} g^{-1}, which is about 1.7 times higher than that of pristine CN nanosheets. The MS measurements determine the band structures of the CN and WO_3 in the heterostructure. The CBM and VBM positions of CN are more negative than those of WO_3. On the other hand, EPR analysis implies the existence of photogenerated electrons in the CB of CN and in the VB of WO_3. Thus, the S-scheme charge transfer mechanism of the WO_3/CN heterojunction is confirmed. Under light irradiation, the photogenerated electrons transfer from the CB of CN to the CB of WO_3 resulting in an IEF and band bending at the interface of the WO_3/CN heterojunction. Both the IEF and band bending accelerate the charge transfer and separation, promoting photocatalytic reduction for H_2 production. Moreover, the interfacial contact can also be moderated to reduce interface contact resistance and facilitate charge migration and separation.[154]

3.2.4 **Other heterostructures.** When n-type CN is in contact with a p-type semiconductor, the electrons will transfer from CN to the p-type semiconductor, resulting in an upward band bending of CN and a downward band bending of the p-type counterpart. Fig. 6a presents the CN/Pt Schottky junction and

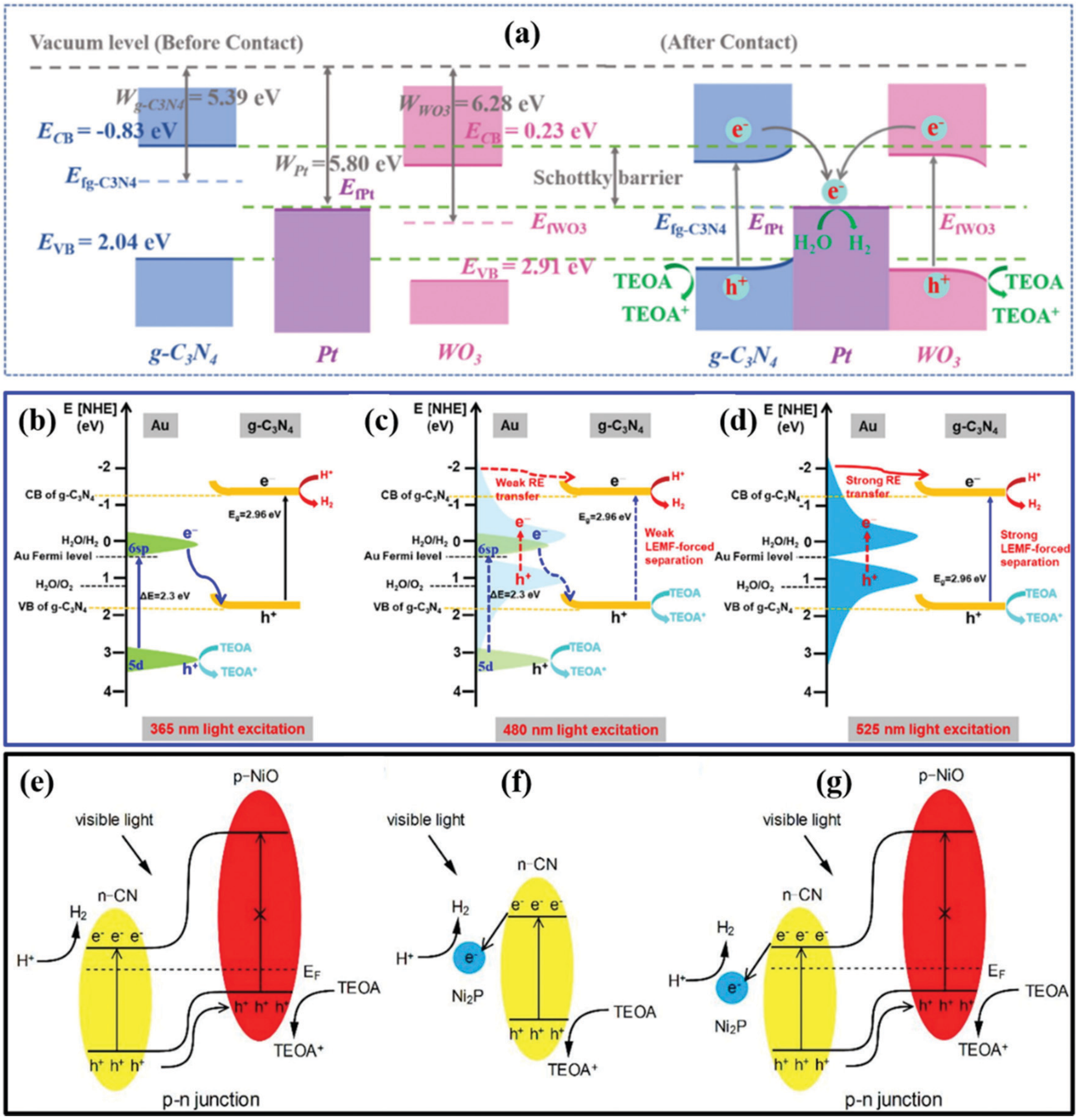

Fig. 6 (a) The photocatalytic H_2 evolution mechanism of the WPC system. Reprinted with permission.[157] Copyright 2021, Elsevier. (b–d) Schematic illustrations of the different mechanisms of SCN/Au5 in producing H_2. Reprinted with permission.[160] Copyright 2020, Elsevier. The separation and transfer of electron–hole pairs in NiO/CN (e), Ni_2P/CN (f), and NiO/Ni_2P/CN (g). Reprinted with permission.[162] Copyright 2019, Elsevier.

Pt/WO_3 ohmic junction. The work function of CN is lower than that of Pt, and the photogenerated electrons diffuse from the CB of CN to the conductor through the contacting interface. An upward energy band bending occurs in CN, forming an electronic barrier (Schottky barrier) at the interface of CN and Pt. The Schottky barrier successfully prevents the recombination of electron–hole pairs from the CB and VB of CN. On the other side, the work function of Pt is smaller than that of WO_3. Thus, the electrons flow from Pt to the CB of WO_3, resulting in a downward band bending of WO_3 and the formation of an ohmic junction. In this case, the electrons can transfer back to the surface of Pt, alleviating the recombination of non-equilibrium carriers. The charge separation can be optimized by constructing the CN/Pt/WO_3 (WPC) ternary heterostructure with both Schottky and ohmic junctions. The Pt with a low overpotential accumulates electrons and absorbs protons for water reduction. Therefore, the WPC Schottky–ohmic junction[157] realized a fruitful H_2 production amount (1299.4 μmol in 5 h) using TEOA as a sacrificial reagent under visible light, which is 11 times higher than that of CN. The intimate Schottky-based heterojunctions of Ni_3C@Ni/CN nanosheets were reported with a high H_2 production rate of 11.28 $\mu mol\ h^{-1}$ in TEOA solution.[158] The photogenerated electrons in the CB of CN transfer to the metallic Ni surface, and the conductive Ni layers rapidly capture electrons and transfer to the Ni_3C core for catalytic H_2 evolution. Owing to the synergy of the Ni_3C, Ni and CN, the highly enhanced photocatalytic performance was achieved.

In addition, the localized surface plasmon resonance (LSPR) effect and inter-band transitions of some metals (such as Ag, Au, and Bi) can largely enhance light absorption.[159] Wang *et al.*[160] reported a SiO_2-CN/Au (SCN) hybrid photocatalyst generating hot carriers for enhanced photocatalytic H_2 production. As presented in Fig. 6b–d, hot electrons that originated from inter-band transitions (d → sp) and LSPR inter-band transitions at the Au surface combined with holes in the VB of SCN. Due to the Schottky barrier, the electrons in the CB of SCN would not transfer back to the Au surface. Spatial charge separation was successfully achieved. The d → sp inter-band transitions occur at energies higher than 2.3 eV. Thus, the d → sp inter-band transitions can be ignored for 525 nm light excitation. The Au nanoparticles of small sizes (lower than ∼2 nm) have stronger inter-band transitions and show relatively weak LSPR absorption than the large Au NPs. By employing small sized Au particles, the AQE driven by the LSPR effect (0.28%) is much lower than that driven by the d → sp inter-band transitions (4.29%) under 525 nm light irradiation.

A p–n heterojunction also has an IEF promoting spatial charge separation.[161] Shi *et al.*[162] synthesized a Ni_2P decorated NiO/CN p–n heterojunction for enhanced photocatalytic H_2 production. As presented in Fig. 6e–g, the IEF helps the separation of electron–hole pairs by driving the holes in the VB of CN to the VB of NiO. The Ni_2P acts as the cocatalyst to capture the electrons and enhance the light absorption. With a low overpotential, the water reduction reaction occurs on the surface of Ni_2P. The NiO/Ni_2P/CN p–n heterostructure exhibited an H_2 evolution rate 126 times higher than that of pristine CN under visible-light irradiation ($\lambda > 420$ nm). The p–n heterojunctions accelerate the charge separation and improve the photocatalytic performance of CN.

3.3 TMD-based heterostructures

The family of TMD materials defined as MX_2 (M = transition metals; X = S, Se or Te) ranges from insulators (group-IV TMDs HfS_2, *etc.*), semiconductors (group-VI TMDs MoS_2 and WS_2, and group-VII TMDs ReS_2, *etc.*), semi-metals (such as $TiSe_2$), to metals (such as group-V TMDs NbS_2 and VSe_2).[163,164] The properties of TMD materials highly depend on the number of d-electrons, chalcogen size and the number of layers. With their tuneable electronic and thermoelectric properties, TMD materials have attracted considerable attention in the application of energy conversion during the past few years.[165–167] The physicochemical properties of TMD materials can be derived from the monolayered unit. The weak vdW force connection between layers results in different structures of TMDs as shown in Fig. 7a. Monolayer TMDs mainly include the trigonal prismatic and octahedral phases (the 1H and 1T phases with D_{3h} and D_{3d} symmetry, respectively). The 1T′ and 1T″ phases are derived from the distorted structures of the 1T phase, while the 2H and 3R phases have resulted from different stacking arrangements of the 1H phase.[168] These physicochemical properties, including the electronic structure, thermodynamic stability, and photocatalytic activity, of TMDs differ in various phases. For example, the trigonal prismatic phases of (Mo,W)S_2 and (Mo,W)Se_2 exhibit better stability than their octahedral phases.[169] The 1T and 2H phases of MoS_2 exhibit superconductivity, magnetism, ferroelectricity and memristive behavior, which could be applied in electronics, catalysis and energy storage.[170] And the 3R-phases of MoS_2 and WS_2 are often considered to be better catalysts compared to the 2H-phases.[171] Fig. 7b summarizes the band structures of conventional semiconductor photocatalysts and TMD materials. Apparently, TMD materials have narrow bandgaps, and absorb a wide range of light energy. With effective light absorption, TMD photoelectrodes are expected to realize promising STH efficiencies higher than those of most traditional metal oxides as illustrated in Fig. 7c. By constructing heterostructures, the CBM and VBM positions of these TMDs can be further modified as shown in Fig. 7d. Therefore, the oxidation and reduction reactions of water splitting can be more feasible.

3.3.1 MoS_2-based heterostructures.

MoS_2 materials are the most well-utilized TMD as electrocatalysts and photocatalysts for H_2 production from water splitting.[173,174] A large number of publications about MoS_2 and MoS_2-based heterostructures applied as photocatalysts are shown in Fig. 8a. Benefiting from the unique and tunable electronic structures of MoS_2, MoS_2-based heterostructures including type II, Z-scheme, and S-scheme heterostructures usually exhibit versatile optical absorption, charge carrier transport and mobility, acceptable conductivity and superior photostability.

Type II heterostructures. Wang *et al.*[175] reported a MoS_2/CN/graphene oxide (GO) ternary nanojunction for effective water splitting as shown in Fig. 8b. The type II MoS_2/CN/GO heterostructure had a band alignment which facilitates collection of

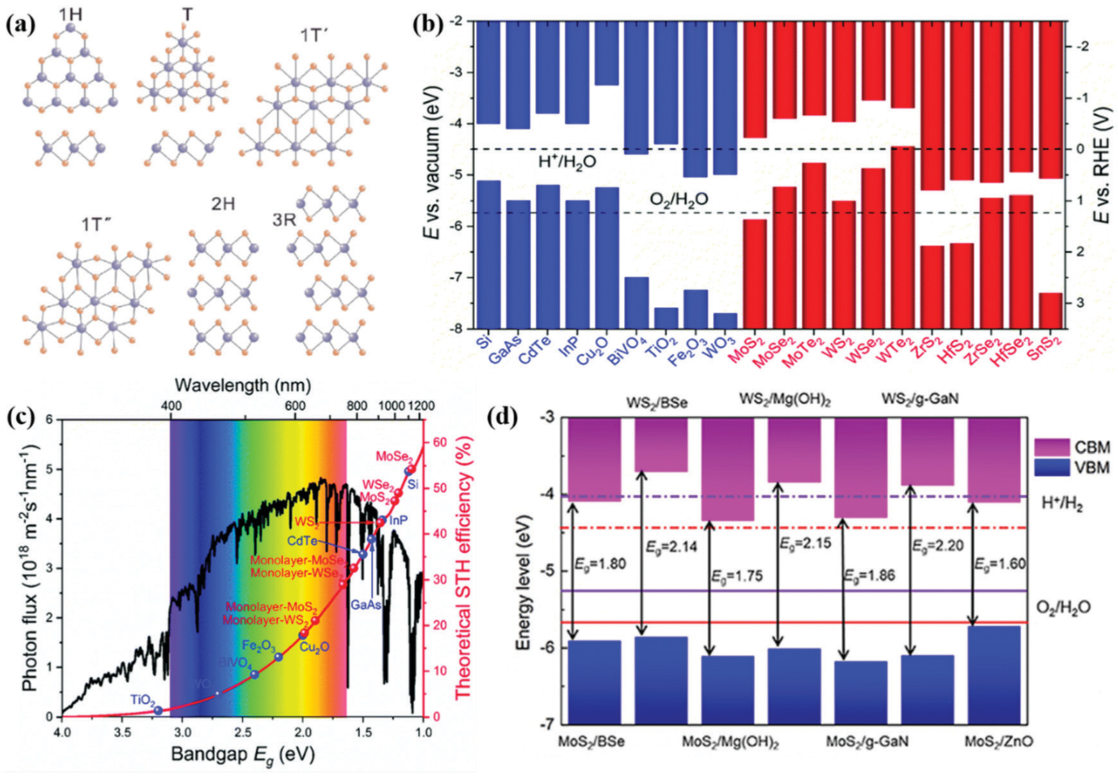

Fig. 7 (a) Structures of 2D TMDs. Reproduced with permission.[172] Copyright 2019, Science in China Press. (b) Band alignments for conventional semiconductors and 2D TMD monolayers. (c) Theoretical maximum solar-to-hydrogen (STH) conversion efficiency as a function of the bandgaps of the semiconductors based on the AM 1.5G solar spectrum, with the assumption that all the semiconductor photoelectrodes have an IPCE of 100% in the absorption range. Reproduced with permission.[166] Copyright 2018, Royal Society of Chemistry. (d) The band structures of some TMD based vdW heterostructures. Reprinted with permission.[38] Copyright 2020, Institute of Physics Publishing.

electrons in MoS_2 and holes in CN as indicated in Fig. 8c. The effective charge transfer and separation allow for retardation of charge recombination. The MoS_2/CN/GO photocatalyst exhibited a highly enhanced H_2 production rate of 1.06 mmol h^{-1} g^{-1} (4.3 times higher than that of MoS_2) using Na_2SO_3 as a sacrificial agent under simulated AM1.5G solar irradiation. The ESI spectra further confirm the efficiency of the trapping, transfer, and separation of charge carriers of the MoS_2/CN/GO heterostructure as illustrated in Fig. 8d. The MoS_2/ZnO vdW heterostructure also constructs a type-II band alignment with a large built-in electric field,[176] which enables enhanced efficiency of optical absorption especially under visible light as shown in Fig. 8e. The type-II MoS_2/GaN heterostructure moves up the band edges of MoS_2 for $\sim$0.5 eV by the deployment of interface nitridation.[177] The increased conduction band offset (CBO) could result in improved capability of electron accumulation on the GaN side. The nitridation interfacial layer in the MoS_2/GaN 2D/3D heterostructure leads to a substantial optical absorption ability and subsequent photocatalytic activity for water splitting using solar energy.

Z-scheme heterostructures. Lu *et al.*[178] synthesized a CN/Ag/MoS_2 ternary plasmonic photocatalyst in a flowerlike architecture forming a Z-scheme heterojunction as shown in Fig. 8f. The Z-scheme-assisted rapid charge separation and suppressed recombination of photoexcited electron–hole pairs significantly boost the photocatalytic H_2 production rate of CN/Ag/MoS_2. The CN/Ag/MoS_2 photocatalyst has an H_2 production rate of 10.40 μmol h^{-1}, which is approximately 8.78 times, 3.51 times and 2.08 times that of Ag/MoS_2, pure CN, and CN/MoS_2, respectively. A solid-state Ag NP-decorated MoS_2/reduced graphene oxide (RGO)/$NiWO_4$ Z-scheme photosystem was constructed.[179] In addition to the Z-scheme function, the RGO mediator and the plasmonic effect of Ag NPs facilitate the charge transfer to enhance photocatalytic efficiency. Nagajyothi *et al.*[180] reported a $ZnFe_2O_4$/MoS_2 Z-scheme heterostructure achieved an H_2 production rate of 142.1 μmol h^{-1} g^{-1}, which is 2.3 times higher than that of pristine MoS_2. The MoS_2/$CaTiO_3$ Z-scheme heterostructure was developed for efficient H_2 production from water splitting. The high transient current density of $ZnFe_2O_4$/MoS_2 verifies the efficient separation of electron–hole pairs. And the low radian impedance of $ZnFe_2O_4$/MoS_2 from EIS analysis further confirmed the inhibited recombination of electron–hole pairs.

S-scheme heterostructures. A MoS_2/CoAl LDH heterostructure was reported with the advantages of the S-scheme heterojunction driving photocatalytic H_2 generation under visible-light irradiation.[181] The IEF across the interface of MoS_2 and CoAl LDH accounts for the rapid detachment of the electron–hole pairs and a strong redox ability. The XPS and DFT results indicate an upward shifted energy band edge of CoAl LDH and a downward

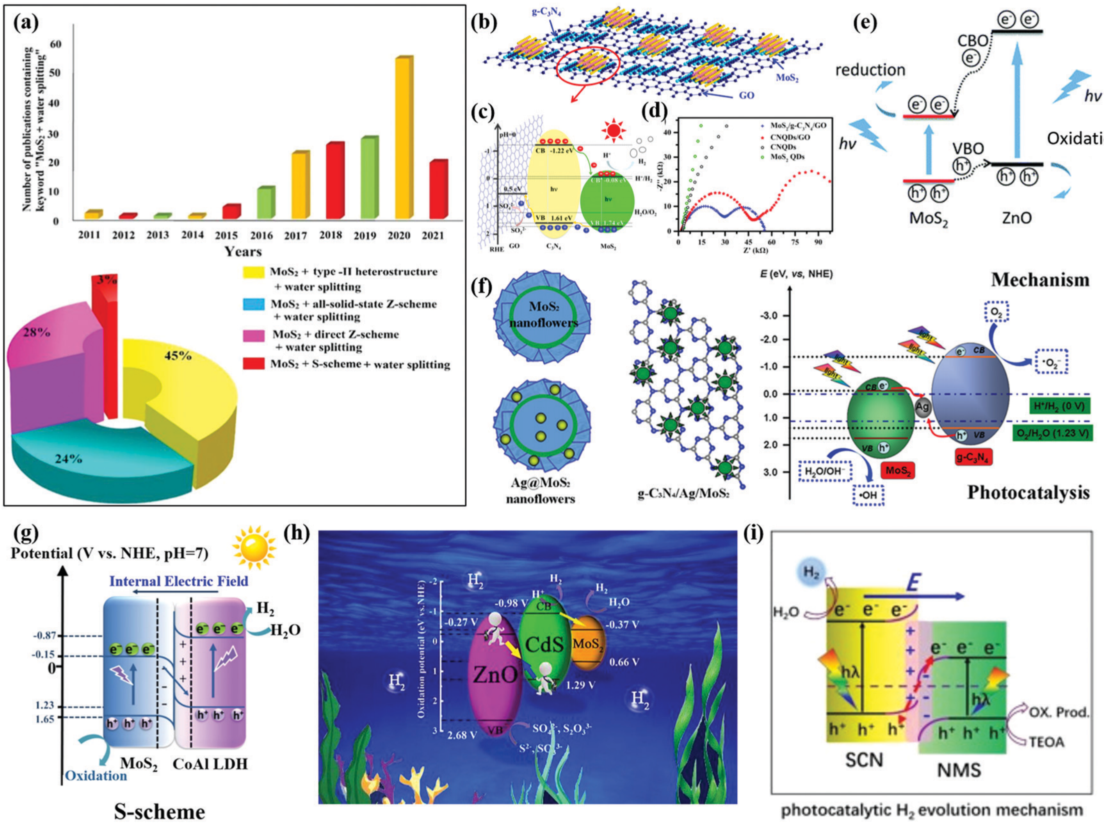

Fig. 8 (a) Number of publications per year on "MoS_2 + photocatalysts" from 2011 to 2021 and different MoS_2-based heterostructure photocatalysts particularly for the application of water splitting photosystems. Reproduced with permission.[183] Copyright 2021, Elsevier. (b) Schematic drawing of the MoS_2/CN/GO composite, (c) schematic illustration of charge carrier separation in a MoS_2/CN/GO junction, and (d) Nyquist plots of these samples. Reprinted with permission.[175] Copyright 2017, American Chemical Society. (e) Schematic illustration of the migration of photogenerated electrons and holes at the MoS_2/ZnO interface. Reprinted with permission.[176] Copyright 2018, Royal Society of Chemistry. (f) Schematic illustration of CN and Ag co-modified MoS_2 nanoflowers and the related photocatalytic mechanism. Reprinted with permission.[178] Copyright 2017, American Chemical Society. (g) S-scheme charge transfer mechanism of the MoS_2/CoAl LDH composite for photocatalytic H_2 generation. Reprinted with permission.[181] Copyright 2021, Elsevier. (h) S-scheme mechanism for the enhanced photocatalytic H_2 evolution. Reprinted with permission.[182] Copyright 2021, Elsevier. (i) S-scheme heterojunction. Reprinted with permission.[156] Copyright 2021, Elsevier.

shifted energy band edge of MoS_2, as illustrated in Fig. 8g. Due to the IEF-induced S-scheme system, the H_2 generation rate of the MoS_2/CoAl LDH could reach 17.1 μmol g^{-1} h^{-1}, which is 8 times that of the pure CoAl LDH. The S-scheme heterojunction not only boosts the charge separation but also allows for the preservation of strong reducibility. Jia *et al.*[182] reported a new S-scheme heterojunction, ZnO/CdS/MoS_2 (ZCM), with suppressed charge recombination and greatly enhanced photocatalytic H_2 evolution performance. As presented in Fig. 8h, the CdS plays as the bridge between ZnO and MoS_2, which promotes charge separation through an intimate interface. The UV-vis diffuse reflectance spectra (DRS) and surface photo-voltage (SPV) spectra prove the strong visible light absorption of the ZCM sample. The transient photocurrent (TPC) spectra and EIS spectra further confirmed the efficient charge separation ability of ZCM. Therefore, the obtained ZCM exhibited superior photocatalytic activity for water splitting over the individual or binary components. An S-scheme heterojunction of N-doped MoS_2 (NMS) and S-doped CN (SCN) was also found to show a high H_2 generation rate of 658.5 μmol g^{-1} h^{-1} (23 and 38 times that of pure SCN and NMS, respectively) using TEOA as a sacrificial reagent. As presented in Fig. 8i, the electrons transfer from SCN with a high Fermi level to NMS with a lower Fermi level, forming an IEF until the Fermi level equilibrium is reached. Thus, the photogenerated electrons in the CB of SCN and the photogenerated holes in the VB of NMS with a maximized redox ability are preserved, while photogenerated holes in the VB of SCN combine with photogenerated electrons in the CB of NMS. Therefore, the driving force for charge transfer and separation provided by the S-scheme leads to highly enhanced photocatalytic activity of the NMS/SCN heterostructure.

3.3.2 WS_2-Based heterostructures.

WS_2 is another representative of TMD materials with similar electronic and optical properties of MoS_2.[184] The bandgap of WS_2 ranges from 1.3 to 2.1 eV depending on its morphology and the number of layers, which makes it a very promising photocatalyst.[185] The construction of heterostructures helps in overcoming the drawbacks of WS_2 based photocatalysts for photocatalytic water splitting.

Type II heterostructures. The photoactivity of wide band gap oxides, such as WO_3 and TiO_2, can be extended to the visible light region by forming type-II heterojunctions with WS_2.[186] Xiao *et al.*[187] reported TiO_2/WS_2 (MoS_2) heterostructures integrating the merits of both components for photocatalytic water splitting under solar light. Notably, the TiO_2/WS_2 (or MoS_2) heterostructures have a type-II band alignment but with a built-in IEF. As shown in Fig. 9a and b, the work function of WS_2 is smaller than that of TiO_2, which results in an electron flow from WS_2 to TiO_2. The formation of the built-in IEF facilitates the migration of carriers. Under solar light irradiation, the photoexcited electrons in the CB of WS_2 transfer to the CB of TiO_2 for the reduction reaction of water splitting. On the other side, the photoexcited holes migrate from the VB of TiO_2 to the VB of WS_2 for the oxidation reaction of water splitting. Therefore, the TiO_2/WS_2 heterostructure achieves the spatial separation of photogenerated electron–hole pairs. The maximum conversion efficiencies for WS_2/TiO_2 and MoS_2/TiO_2 could reach 11.5% and 13.5%, respectively, according to the DFT calculation.

Z-scheme heterostructures. WS_2 based Z-scheme heterojunctions offered excellent H_2 production from photocatalytic water splitting by optimization of pristine WS_2, including the recombination of charge pairs, active centres and photostability.[188] Xue *et al.*[189] constructed a direct Z-scheme $WO_3/WS_2/CdS$ tandem heterojunction with a high photocatalytic H_2 evolution rate of 14.34 mmol h^{-1} g^{-1} and an outstanding apparent quantum efficiency (AQE) of 22.96% at 435 nm as shown in Fig. 9c and d. The electrons transfer from the CB of CdS to the CB of adjacent WO_3 and WS_2, forming a dual built-in IEF at the heterointerfaces of the WS_2/CdS and WO_3/CdS. The *in situ* irradiated XPS (ISI-XPS) measurement and ultraviolet photoelectron spectral (UPS) analysis results confirmed the route of interfacial charge transfer in the hybrid system. Apparently, the energy-level alignment of the direct Z-scheme system facilitates the spatial separation for enhanced H_2 production performance. A WS_2/MoS_2 in-plane few-layer heterostructure was reported with rapid charge separation and a promising H_2 generation rate of 9.83 mmol g^{-1} h^{-1}.[190] As presented in Fig. 9e and f, the WS_2 and MoS_2 are located in the upper and lower parts of the images, respectively. Due to the difference of atomic numbers in WS_2 and MoS_2, the interface of the two materials is distinguishable. The WS_2/MoS_2 heterostructure forms a type II heterojunction as shown in Fig. 9g, acting as an electron sink to prevent the recombination of electron–hole pairs. Thus, the WS_2/MoS_2 heterostructure exhibits much higher photocatalytic activity than the individual components.

3.3.3 Other TMD-based heterostructures. Transition metal selenides (TM-Se) and tellurides (TM-Te) are less studied for

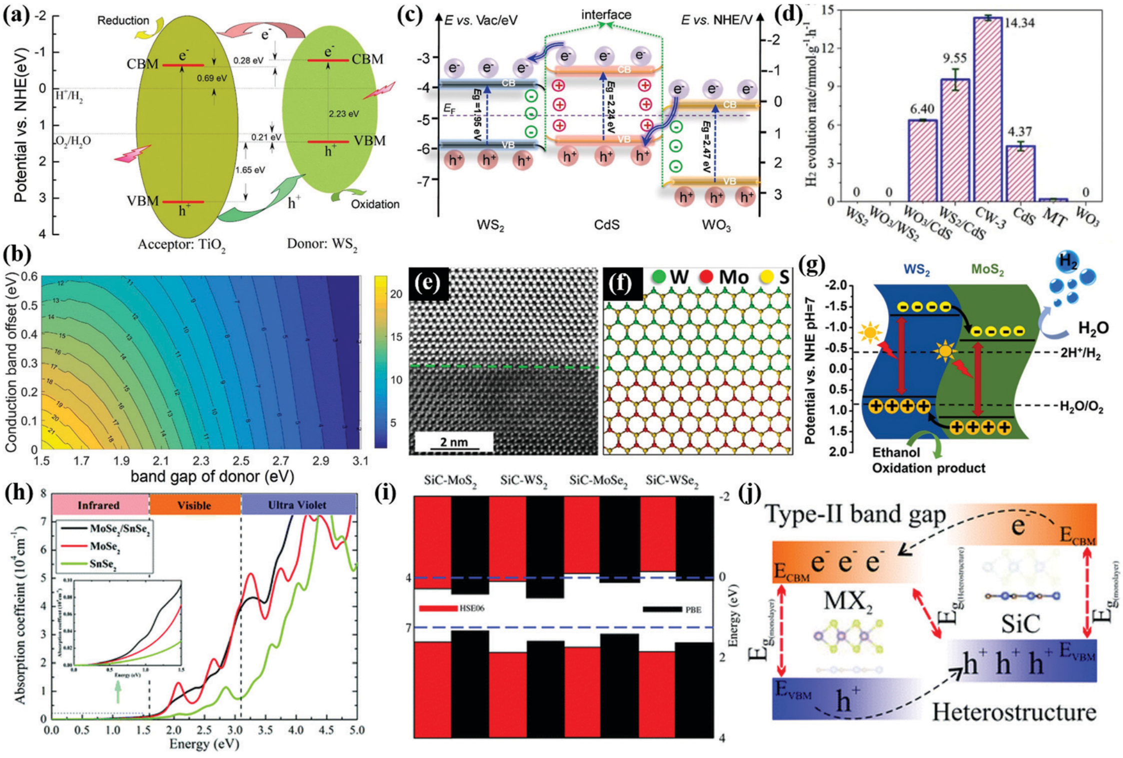

Fig. 9 (a) Schematic illustration of type-II band-alignments in the WS_2/TiO_2 heterojunction. (b) Contour plots showing the energy-conversion efficiency *versus* the donor bandgap and the conduction band offset. All the energy levels are referenced to the reduction (H^+/H_2) potential. Reprinted with permission.[187] Copyright 2020, Elsevier. (c) Charge transfer behavior of the CW heterostructure, (d) H_2 evolution rates over different samples under visible light irradiation ($\lambda > 420$ nm). Reprinted with permission.[189] Copyright 2020, Elsevier. (e) The top part is the WS_2, while the bottom is the MoS_2. (f) Atomic model of the WS_2–MoS_2 interface. (g) Schematic representation of the proposed mechanism for photocatalytic H_2 evolution over a WS_2–MoS_2 heterostructure. Reproduced with permission.[190] Copyright 2021, Elsevier. (h) Calculated absorption coefficients of the $MoSe_2$ (WSe_2), $SnSe_2$ monolayer, and $MoSe_2/SnSe_2$ ($WSe_2/SnSe_2$) heterostructure. Reprinted with permission.[191] Copyright 2019, Royal Society of Chemistry. (i) VBM and CBM for the heterostructures. (j) Type-II band alignment in heterostructures. Reprinted with permission.[192] Copyright 2018, Royal Society of Chemistry.

photocatalysis due to their rareness and limitation on band structure.[193–195] Although experimental research work about TM-Se and TM-Te based heterostructures for photocatalytic water splitting is limited, the theoretical calculation predicted the great application potential of TM-Se and TM-Te based heterostructures in photocatalysis for H_2 production. Fan *et al.*[191] proposed $MoSe_2/SnSe_2$ and $WSe_2/SnSe_2$ heterostructures for photocatalytic overall water splitting using DFT calculation. The $MoSe_2/SnSe_2$ and $WSe_2/SnSe_2$ heterostructures could form direct Z-scheme photocatalytic systems with reduction reaction and oxidation reaction occurring on the $MoSe_2$ (WSe_2) and $SnSe_2$, respectively. The optical properties of the heterostructures were evaluated using the complex dielectric function of DFT-HSE06 as shown in Fig. 9h. Apparently, the heterostructure absorbs a wide range of light up to the visible and infrared regions compared to the individual components. The red-shifted absorption edge can be attributed to the electronic state hybridization of $MoSe_2$ (WSe_2) and $SnSe_2$. The improved light absorption abilities of the $MoSe_2$ (WSe_2) and $SnSe_2$ heterostructures could result in high STH efficiencies up to 10.5%. Din *et al.*[192] provided comprehensive insights into the electronic structures, and optical and photocatalytic performance of SiC-MX_2 type-II heterostructures. The photogenerated electrons in SiC transfer to the MX_2 layer, while holes in MX_2 migrate to the SiC layer. The effective charge transfer and separation could be realized in the SiC-MX_2 heterostructures. The calculated band gap structures of SiC-MX_2 heterostructures using the Perdew–Burke–Ernzerhof (PBE) and HSE06 functionals are presented in Fig. 9i. From the HSE06 functional results, the VBMs of the SiC-Mo(W)S_2 heterostructures are lower than the oxidation potentials, while the CBMs of the SiC-Mo(W)Se_2 heterostructures are higher than the redox potentials. Therefore, the SiC-Mo(W)Se_2 heterostructures have great potential for photocatalytic water splitting.

3.4 LDH-based heterostructures

LDH materials consist of brucite like metal hydroxide layers and water molecules balanced by interlayer anions[196,197] as shown in Fig. 10a. The general formula of an LDH can be expressed as

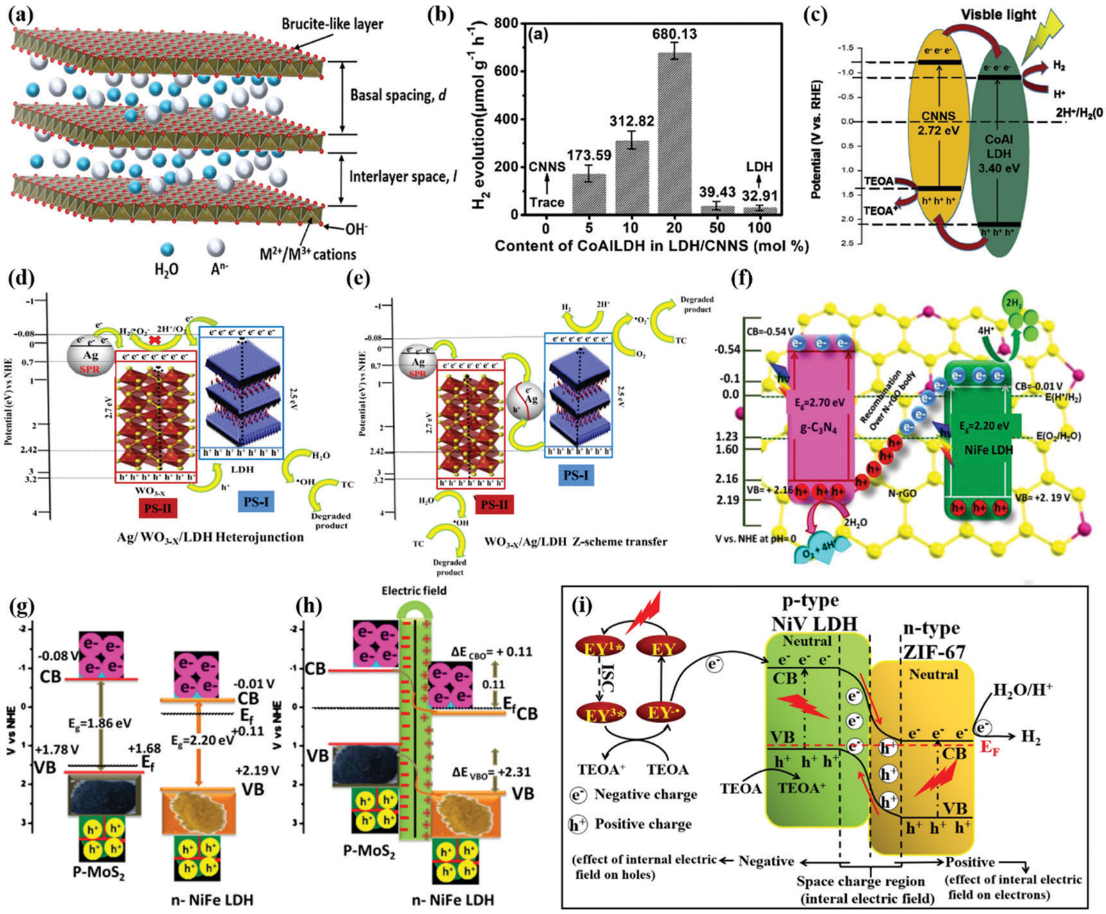

Fig. 10 (a) Representative structure of LDH materials. Reprinted with permission.[198] Copyright 2022, Elsevier. (b) The H_2 evolution efficiency with different ratios of CoAl-LDH loading on the CNNS. (c) Mechanism for hydrogen evolution over CoAl-LDH/CNNS under visible light irradiation. Reprinted with permission.[202] Copyright 2020, Elsevier. Schematic illustration of the proposed reaction mechanism in the (d) Ag/WO_{3-x}/LDH heterostructure and (e) WO_{3-x}/Ag/LDH-based reaction systems toward TC degradation and H_2 evolution under visible light irradiation. Reprinted with permission.[209] Copyright 2019, American Chemical Society. (f) Z-scheme mechanism for mineralization of dyes with H_2 and O_2 evolution over the CNNG3LDH heterostructure. Reprinted with permission.[210] Copyright 2019, Nature. (g and h) Potential edge alignment for n-type NiFe LDH and p-type MoS_2. Reprinted with permission.[218] Copyright 2019, American Chemical Society. (i) Internal migration mechanism of electrons in the p–n junction. Reprinted with permission.[221] Copyright 2020, Elsevier.

$[M^{2+}_{(1-x)}M^{3+}_{x}(OH)_2]^{x+}(A^{n-})_{x/n}\cdot mH_2O$, where M^{2+} and M^{3+} represent bivalent (Mg^{2+}, Cu^{2+}, Zn^{2+}, Mn^{2+}) and trivalent (Al^{3+}, Fe^{3+}, Ti^{3+}, Cr^{3+}) cations, respectively. A^{n-} is the interlayer anion of valence n (CO_3^{2-}, SO_4^{2-}, NO_3^{-}, Cl^{-}, F^{-}, *etc.*) and x (0.2–0.4) represents the molar ratio of trivalent cations to the total cation content. LDH materials have high adsorption capacity, tunable bandgaps, and abundant reaction sites for water splitting reactions.[198] Moreover, the rich components and various derivatives make LDHs flexible to construct heterostructures with different semiconductors and cocatalysts such as CN, TiO_2, CdS, and some noble metals.[199–201]

3.4.1 Type II heterostructures. By forming type-II heterojunctions with other semiconductors especially with visible-light response and good transportation capacity, the photocatalytic activity of LDH materials can be highly enhanced. Zhang *et al.*[202] coupled CoAl-LDH with CN nanosheets (CNNS) forming an LDH/CNNS heterojunction (type-II heterojunction) for highly enhanced photocatalytic H_2 production. Fig. 10b presents the H_2 production rates of LDH/CNNS samples with different loading amounts of CoAl-LDH. With 20 mol% CoAl-LDH in CNNS, a remarkable photocatalytic H_2 evolution rate of 680.13 μmol h^{-1} g^{-1} was realized, which was 21 times higher than that of pure CoAl-LDH (32.91 μmol h^{-1} g^{-1}). The EIS and PL spectra proved the efficient charge transfer and inhibited recombination of electron–hole pairs in the LDH/CNNS hybrid. The MS plots and the UV-vis reflectance spectra further determined the band structure of LDH/CNNS. The type-II heterojunction assisted photocatalytic mechanism was confirmed as illustrated in Fig. 10c. The CoO/NiCo-LDH type-II heterojunction was also reported[203] to achieve an outstanding photocatalytic H_2 production efficiency and long-term photostability. SPV measurement indicated the efficient diffusion process of photogenerated charges in CoO/NiCo-LDH. In the type-II heterojunction, the photogenerated holes from the VB of NiCo-LDH transfer to the VB of CoO and then are consumed by the hole scavengers (Na_2SO_3 and Na_2S). Due to the synergy of improved light absorption and type-II heterojunction-driven charge separation, the photocatalytic activity for H_2 production is highly enhanced.

CdS also forms type-II heterojunctions with LDH materials.[204] Li *et al.*[205] reported a novel type-II heterojunction based on NiCo-LDH/P doped CdS (P-CdS) with an H_2 production rate of 8.665 mmol h^{-1} g^{-1} under visible light, which was 45 times higher than that of pure CdS. The DFT results indicated that the work function value of P-CdS is higher than that of NiCo-LDH, leading to an electron flow from NiCo-LDH to CdS. The space charge layer and IEF at the interface between NiCo-LDH and CdS help the charge separation. In addition, the P doping induces a mid-gap between the CB and VB of CdS, trapping photogenerated electrons. Due to the synergy of the NiCo-LDH/P-CdS heterostructure, the efficiency of photocatalytic H_2 production was highly enhanced. Zhou *et al.*[199] *in situ* synthesized CdS on the surface of NiFe LDH, forming a nanoscale heterojunction. The TPR results of the CdS/NiFe LDH clearly showed a reduced onset potential and increased photocurrent density. The efficient separation of photogenerated electron–hole pairs was confirmed in the CdS/NiFe LDH due to the type II band alignment between the CdS and NiFe LDH. The NiFe LDH acted as an electron sink absorbing protons and accumulating electrons for the HER. Thus, the CdS/NiFe LDH exhibited notable H_2 evolution kinetics (469 μmol h^{-1} g^{-1}), which was much higher than those of individual CdS and NiFe LDH.

3.4.2 Z-scheme heterostructures. LDH-based Z-scheme heterostructures with strong redox abilities and efficient charge separation have been widely employed as photocatalysts for H_2 production.[206–208] Sahoo *et al.*[209] reported a WO_{3-x}/Ag/ZnCr LDH ternary heterostructure where Ag nanoparticles act as the solid-state electron mediator. Because of the positive CB potential of WO_{3-x} (0.7 V *vs.* NHE) determined by MS and Tauc plots, the electrons in the CB of WO_{3-x} are not able to reduce H_2O to H_2 as shown in Fig. 10d. Thus, the excellent visible light-driven H_2 evolution of the WO_{3-x}/Ag/ZnCr LDH heterostructure was attributed to the formation of a Z-scheme heterojunction instead of a conventional type-II heterojunction as illustrated in Fig. 10e. The metallic Ag nanoparticles not only enhance the absorption of visible light due to their SPR effect but also improve the interfacial charge migration between WO_{3-x} and ZnCr LDH. Other conductive materials such as graphene derivatives and reduced graphene oxides (rGOs) can also work as electron mediators to boost the charge transfer and separation. Nayak *et al.* introduced the negatively charged N doped rGO (NrGO) to the self-assembled interface of the CN/NiFe LDH hybrid.[210] The sample with 3 wt% GO in the CN/NiFe LDH (CNNG3LDH) exhibited the best photocatalytic performance under visible light compared to reference samples. The Z-scheme assisted charge transfer route is illustrated in Fig. 11f. With the help of conductive rGO, the holes from the VB of CN combine with electrons from the CB of NiFe LDH, inhibiting the recombination of photogenerated electron–hole pairs on the individual CN and NiFe LDH. The low PL intensity, small arc of the Nyquist plot (43.8 Ω) and high photocurrent density of CNNG3LDH all revealed effective charge transfer and separation in the CN/rGO/NiFe LDH heterostructure. Moreover, the TRPL spectra proved the prolonged lifetime of electron–hole pairs in CNNG3LDH.

Ternary heterostructures with two Z-scheme channels for enhanced photocatalytic H_2 production are often reported.[211,212] Megala *et al.* synthesised NiAl-LDH/CN/Ag_3PO_4 (AP) ternary composites, where CN has the lowest CB potential and AP has the highest VB potential, which result in a strong redox ability.[213] In the dual Z-scheme, the holes from the lower potential VB combine with electrons from the higher potential CB, which separates photogenerated electron–hole pairs. The electrons from the lowest potential CB reduce protons to H_2 and those from the highest CB potential VB oxidise water into O_2. By band alignment between NiAl-LDH, CN, and AP, the most efficient charge transfer route can be achieved, leading to high photocatalytic performance.

The interface charge transfer between the two components in the Z-scheme system is a crucible for the separation and subsequent migration of photogenerated electron–hole pairs.[214] A donor–bridge–acceptor structure bonding two components at atomic and electronic levels in a heterostructure can optimize the charge migration at the heterojunction interface.[215] Wang *et al.* constructed a covalent-bonding-bridge structure at the

Cu_2O@ZnCr-LDH heterointerface, with a thin-layer Cu_2O core and a $S_2O_3^{2-}$ anion intercalated ZnCr-LDH shell.[208] The extended X-ray absorption fine structure (EXAFS) fitting and coincidence Doppler broadened positron annihilation spectroscopy (CDB-PAS) confirmed the formation of a $Cu^{-}(S_2O_3^{2-})$/LDH bridge structure and its function at the heterointerface. The bridge-type bonding helps the passage of carriers and promotes the charge transfer, which thus highly enhances the utilization of photogenerated carriers. The transient current–potential measurement and PL spectra further revealed improved charge transfer efficiency of photoexcited carriers in the Cu_2O@ZnCr-LDH heterostructure. Thus, the Cu_2O@ZnCr-LDH heterostructure displayed an acceptable H_2 production rate from pure water without using any co-catalysts under visible light.

3.4.3 p–n heterostructures. The p–n junction generates a space charge region, resulting in a strong IEF, which is beneficial to charge separation of photogenerated electron–hole pairs.[216,217] Nayak *et al.*[218] composited p-type MoS_2 with n-type NiFe LDH applied in photocatalysis. Due to the work function and Fermi level differences in MoS_2 and NiFe LDH as shown in

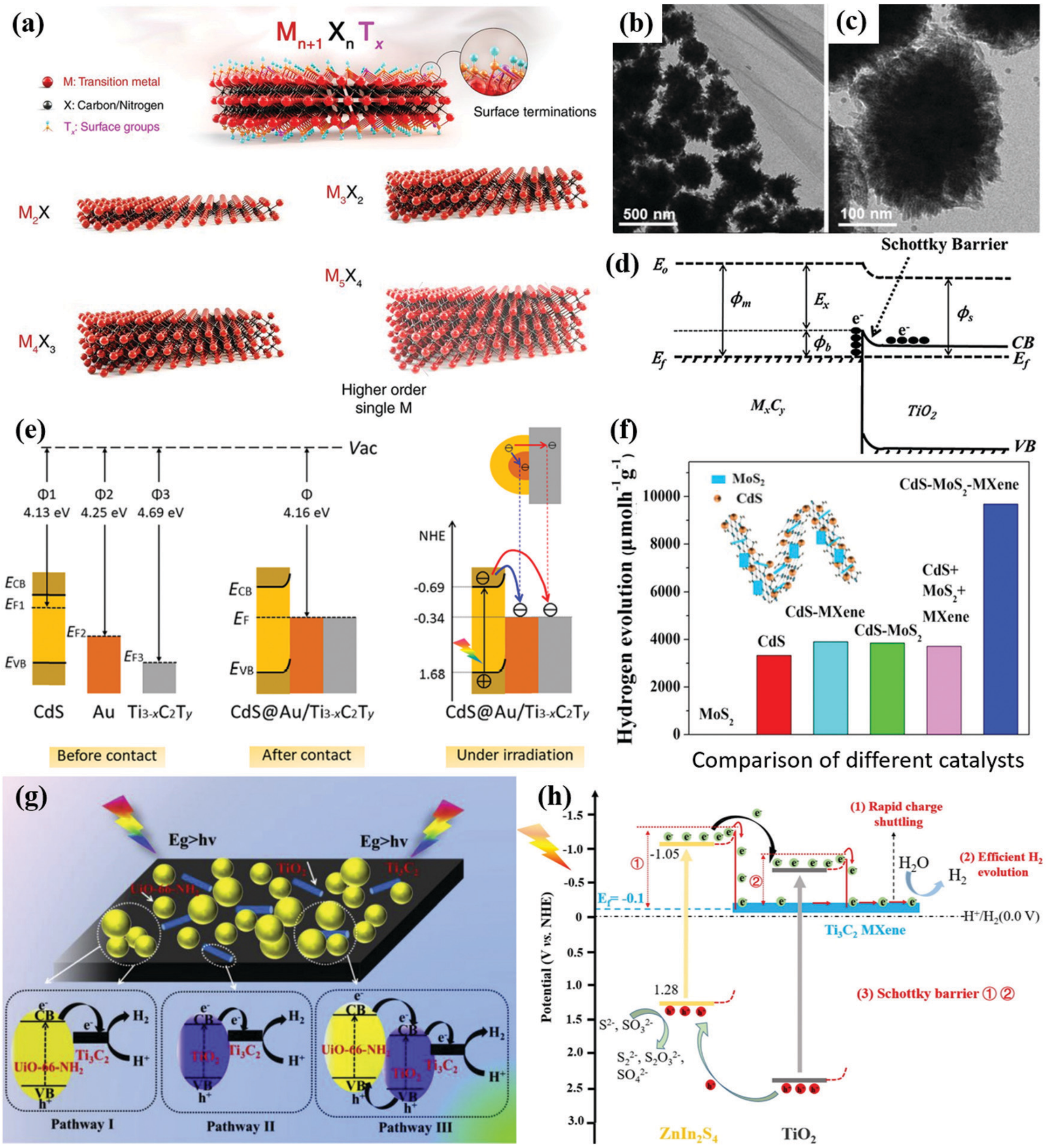

Fig. 11 (a) Schematic illustration of the MXene structures. Reproduced with permission.[238] Copyright 2021, Science. (b and c) TEM images of TiO_2/$Ti_3C_2T_x$ (5 wt%). (d) Formation of a Schottky barrier at the MXene/TiO_2 interface. Reprinted with permission.[231] Copyright 2016, Wiley-VCH. (e) Energy level diagram and the photogenerated charge carrier transfer process of CdS, Au, and $Ti_{3-x}C_2T_y$. Reprinted with permission.[234] Copyright 2021, American Chemical Society. (f) Photocatalytic H_2 evolution over different catalysts. Reprinted with permission.[235] Copyright 2019, Elsevier. (g) Schematic illustration of the charge-transfer pathways for Ti_3C_2/TiO_2/UiO-66-NH_2. Reprinted with permission.[236] Copyright 2019, Elsevier. (h) Proposed process of photoinduced charge transfer process on the M@T/ZIS-50 ternary hybrid. Reprinted with permission.[237] Copyright 2020, Elsevier.

Fig. 11g and h, electrons flow from the CB of NiFe LDH to MoS_2, which leads to downward band shifting and upward band shifting of MoS_2 and NiFe LDH, respectively. The space charge region and built-in IEF at the heterojunction interface prevent the recombination of electron–hole pairs and accelerate the mass transport. In addition, the charge transfer follows the Z-scheme route for the photocatalytic reactions. Electrons accumulated in the CB of p-type MoS_2 for the HER. Both the chemical kinetics and carrier migration are facilitated by the p-n junctions, leading to an enhanced photocatalytic H_2 production rate of 3 wt% MoS_2 loaded NiFe LDH (550.9 μmol h^{-1}), which is 10.9 and 19.2 times that of NiFe-LDH and MoS_2, respectively.

Cobalt-based semiconductors such as Co_3O_4, CoO and $Co(OH)_2$ are typical p-type semiconductors with attractive electronic properties and narrow band gaps (about 1.2–2.1 eV). By constructing heterojunctions with n-type LDH materials, the disadvantages of Co-based catalysts, such as low light harvesting efficiency and charge transfer capability, can be compensated for. Sahoo *et al.*[219] coupled $Co(OH)_2$ (CH) platelets with an n-type ZnCr LDH, achieving remarkable photocatalytic performance. The MS plots determined the p–n heterojunction in the CH/ZnCr LDH heterostructure. The EIS spectra and photocurrent response proved the efficient charge transfer and separation in the heterostructure. High electron/hole densities are found in the CB of the LDH and the VB of CH, respectively. These concentrated electrons/holes take part in water reduction for H_2 production and water oxidation for O_2 evolution, respectively.

A Co-based zeolitic imidazolate framework (ZIF-67) is another p-type catalyst with large surface area and rich active sites for the HER under visible light irradiation.[220] Wang *et al.*[221] constructed a p–n heterojunction of ZIF-67 and NiV LDH, showing excellent photocatalytic performances for the HER. The ZIF-67/NiV LDH heterostructure had large specific surface area and enhanced light absorption. The photocurrent density of ZIF-67/NiV LDH indicated the high efficiency of separation and migration of photogenerated charges. Owing to the space charge region and IEF at the interface of the p–n junction as shown in Fig. 11i, the charge transfer is accelerated and the recombination of electron–hole pairs is suppressed. The high-density electrons in the CB of ZIF-67 react with protons to produce H_2, while the sacrificial reagent TEOA consumes high-density holes in the VB of NiV LDH. With multiple advantages, the ZIF-67/NiV LDH heterostructure shows a superior photocatalytic H_2 evolution rate, which is 9.5 and 5.9 times higher than those of ZIF-67 and NiV LDH, respectively.

3.5 MXene-based heterostructures

The large MXene family has been proved to be the one of the most attractive photocatalysts with multiple virtues of large interlayer spacing, nontoxicity, large surface area, superior chemical stability, outstanding oxidation resistance, *etc.*[222–224] The general formula of MXenes is $M_{n+1}X_nT_x$ (n = 1–4), where M represents a transition metal (such as Ti, V, Cr, Nb, and Mo), X stands for carbon and/or nitrogen elements, and T_x represents terminal groups (such as O, OH, and F) depending on the synthesis methods as shown in Fig. 11a. For example, the complete oxygen- or chlorine-terminated titanium carbide MXene with two layers of transition metal (n = 1) can be written as Ti_2CO_2 or Ti_2CCl_2, respectively.[225] The strong interaction through the bonding group successfully avoids cleavage fractures, resulting in a unique 2D structure with novel properties.[226] Even though most MXene materials are semiconductors with indirect bandgaps, MXene based heterostructures with other photoactive materials such as TiO_2, CdS, and CN exhibit efficient charge transfer, long-term chemical stability and photocatalytic activity.[227–229]

$Ti_3C_2T_x$ materials were the first and the most investigated MXene materials applied in photocatalysis with a good hydrophilic ability, electrical conductivity, tunable bandgaps in the visible region, and ultrahigh catalytic activity towards the HER.[230] Wang *et al.*[231] reported $Ti_3C_2T_x$ materials encapsulated within TiO_2 nanoparticles as shown in Fig. 11b and c. Due to the rapid charge transfer from TiO_2 to $Ti_3C_2T_x$, the $Ti_3C_2T_x/TiO_2$ heterostructure showed a remarkably H_2 yield. The conductive $Ti_3C_2T_x$ can serve as an electron sink attracting electrons from the CB of TiO_2. The Schottky barrier would form at the interface of $Ti_3C_2T_x$ and TiO_2, which improves the charge separation as illustrated in Fig. 11d. Ultra-thin Ti_3C_2 nanosheets can provide versatile platforms for photocatalytic reactions with large surface areas and abundant surface-active sites. The CdS–$Ti_3C_2T_x$ heterostructure was also reported for enhanced photocatalytic H_2 production under visible light.[232] The matched energy level alignment and intimate interfacial contact between conductive $Ti_3C_2T_x$ and CdS allow rapid charge transfer and enhanced charge separation.[233]

Ultrathin $Ti_{3-x}C_2T_y$ (where x refers to the Ti defects and T_y refers to the surface functional groups) with reductive Ti vacancies was composited with CdS@Au core–shell nanojunctions.[234] In the $Ti_{3-x}C_2T_y$/CdS/Au ternary heterostructure, the work function values follow the order: CdS (4.69 eV) $>$ Au (4.25 eV) $>$ $Ti_{3-x}C_2T_y$ (4.13 eV). Thus, the photogenerated electrons in the CB of CdS transfer to Au and $Ti_{3-x}C_2T_y$, resulting in dual Schottky barriers at the CdS/Au and CdS/MXene interfaces as illustrated in Fig. 11e. The Au and $Ti_{3-x}C_2T_y$ successfully trap the electrons and inhibit the recombination of electron–hole pairs. The metallic Au nanoparticles transmit electrons to the ultrathin layered MXene for the HER. The transient photocurrent response (TPR) and EIS measurements further confirmed the rapid charge transfer and efficient charge separation in the $Ti_{3-x}C_2T_y$/CdS/Au system. With 1.0 wt% $Ti_{3-x}C_2T_y$ and 0.1 wt% Au in CdS, the ternary composites achieved an H_2 production rate of 5371 μmol g^{-1} h^{-1} under visible-light irradiation in lactic acid aqueous solution, which is approximately 26.6 times higher than that of pristine CdS. Another ternary composite, CdS–MoS_2–MXene ($Ti_3C_2T_x$),[235] also exhibited a prominent H_2 production rate of 9679 μmol g^{-1} h^{-1} under visible light ($\lambda \geq 420$ nm) irradiation, which is much higher than those of the bare components and a physical mixture of the three components as shown in Fig. 11f. Due to the high carrier mobility of MXenes, the effective transmission of electrons to MoS_2 and CdS for HER reactions can be realized. MXene materials significantly facilitate the separation of photoexcited electron–hole pairs and the subsequent HER reactions.

Ti_3C_2 MXene materials can maintain their layered structure after a facile annealing process but also provide Ti to form TiO_2 as a new platform for photocatalytic reactions. TiO_2 originated from Ti_3C_2 MXene in close contact with metallic Ti_3C_2, which benefits the rapid transfer of photogenerated charges. By introducing annealed $Ti_3C_2T_x$ MXenes over water-stable Zr-MOFs (UiO-66-NH_2), the Ti_3C_2/TiO_2/UiO-66-NH_2 ternary heterostructure was obtained.[236] Fig. 11g presents the possible contact interfaces including Ti_3C_2/UiO-66-NH_2 and Ti_3C_2/TiO_2 Schottky junctions in Ti_3C_2/TiO_2/UiO-66-NH_2. The photogenerated electrons in the CB of UiO-66-NH_2 and TiO_2 can separately transfer to Ti_3C_2 following pathways I and II, respectively. Since the UiO-66-NH_2 has a higher CB position than TiO_2, photogenerated electrons in the CB of UiO-66-NH_2 can migrate to the CB of TiO_2 first and then to Ti_3C_2 following pathway III. Owing to the synergistic effects of Schottky junctions of Ti_3C_2/UiO-66-NH_2, Ti_3C_2/TiO_2 in Ti_3C_2/TiO_2/UiO-66-NH_2, the photocatalytic H_2 performance of Ti_3C_2/TiO_2/UiO-66-NH_2 reached 1980 μmol h^{-1} g^{-1}, which is 2.1 times higher than that of pristine UiO-66-NH_2 under simulated sunlight irradiation. Huang *et al.*[237] also *in situ* synthesized a Ti_3C_2 MXene embedded with TiO_2 nanosheets (M@TiO_2). By compositing M@TiO_2 with $ZnIn_2S_4$ (ZIS), a type-II heterojunction of ZIS and TiO_2 and a Schottky junction of ZIS and metallic Ti_3C_2 were formed as shown in Fig. 11h. The obtained Ti_3C_2@TiO_2/ZIS ternary heterostructure exhibited superior visible light absorption, and charge separation and transfer. Therefore, Ti_3C_2@TiO_2/ZIS achieved a high photocatalytic H_2 production rate of 1185.8 μmol g^{-1} h^{-1}, which is 9.1 and 4.6 times higher than those of M@TiO_2 and pure ZIS, respectively.

$Ti_3C_2T_x$ as a typical MXene material shows remarkable photocatalytic properties for H_2 production when composited with other semiconductors. The MXene based heterostructures often exhibit rapid charge transfer and separation due to the function of the Schottky junction and synergy with the component cocatalysts.

3.6 Other 2D layered materials

Bismuth oxyhalides (BiOX, X = Cl, Br, and I) are also considered as superior photocatalysts owing to their layered structure and excellent physicochemical properties.[239,240] However, most BiOX photocatalysts are applied in photocatalytic degradation of pollutants or water treatment. The positive CB positions of BiOX highly limit their applications for photocatalytic H_2 production. By constructing heterostructures with semiconductors that have strong reduction power, effective photocatalytic H_2 production over BiOX can be realized. Liu *et al.*[241] synthesized novel SnO/BiOX bilayer heterojunctions with narrow band gaps and type-II band alignment. The HSE06 hybrid DFT results confirm that the band structures of SnO/BiOCl and SnO/BiOBr bilayers are desirable for the redox water-splitting reactions as shown in Fig. 12a. The type-II heterojunctions with an IEF facilitate charge separation as illustrated in Fig. 12b. SnO/BiOCl and SnO/BiOBr heterostructures with strong optical absorption of solar light, engineered band gaps, and improved charge transfer exhibit remarkably enhanced photocatalytic activity for water splitting.

Many new classes of 2D materials have emerged, such as group III nitrides (AlN and GaN), group-III metal monochalcogenides, MX (M = Ga, In, X = S, Se), and metal phosphorus trichalcogenides (MPTs) with large potential application in solar energy conversion.[242–244] For instance, AlN and GaN have hexagonal crystal structures and only 2% lattice mismatch with MoS_2. AlN or GaN and MoS_2 could form intimate heterostructures as reported by Liao *et al.*[245] The band structure characterization determines that MoS_2/AlN and MoS_2/GaN vdW heterostructures have narrow band gaps of 1.62 and 1.52 eV, respectively. And the CBM originates from the Mo d_{z^2} states in the MoS_2 monolayer, which is more negative than the water reduction potential as shown in Fig. 12c. The VBM results from the N p_z states in the AlN(GaN) monolayer are more positive than the water oxidation potential. Therefore, both the optical absorption and water splitting reactions can be facilitated in the AlN(GaN)/MoS_2 heterostructure.

As illustrated in Fig. 12d, single-layer group-III monochalcogenides all have low formation energies like MoS_2, which are suitable for photocatalytic water splitting reactions.[49] Singh *et al.*246 reported a GaS/BTe type-II vdW heterostructure with a large electric field at the heterointerface. The existence of the transverse electric field from 1.0 to 1.0 eV $Å^{-1}$ effectively achieves the band alignment of the heterostructure and improves optical absorption in the visible light region. Fig. 12e presents the charge transfer process in the heterostructure. The photogenerated electrons in the CB of BTe migrate to the CB of the GaS, while the holes in the VB of GaS transfer to the VB of BTe. The efficient charge transfer route in the GaS/BTe heterojunction is beneficial to the HER. Thus, the GaS/BTe heterostructure could exhibit better photocatalytic performance for H_2 production than the individual components.

MPTs include $M^{II}PX_3$ such as $FePS_3$, $NiPS_3$, and $CoPSe_3$ and $M^{I}M^{III}P_2X_6$ (X represents S and Se) such as $CuInP_2S_6$, $AgAlP_2Se_6$, and $AgInP_2S_6$,[242,247] which are known as ferroelectric materials with hexagonal lamellar structures and spontaneous electric polarization. Huang *et al.*[244] demonstrated that ferroelectric vdW heterostructures can result in type-II band alignment by switching the direction of polarization *via* an electric field. Both visible light absorption and charge separation can be improved in $CuInP_2S_6$ (CIPS)/$Mn_2P_2S_6$ and $CuInP_2S_6$/$Zn_2P_2Se_6$ ferroelectric heterostructures. The inherent polarization electric field of MPTs can promote fast transfer and spatial separation of charge carriers, which are promising virtues for photocatalytic water splitting. A CIPS/CN type-II heterojunction was constructed as a photocatalyst for H_2 production (see Fig. 12f and g). The unique 2D/2D CIPS/CN heterojunction with $CuInP_2S_6$ nanosheets loaded onto the surfaces of the CN ultrathin flakes as shown in Fig. 12h and i is beneficial to the surface mass transport and charge transfer of the composite system. Owing to the synergy of the IEF and type-II band alignment, the H_2 evolution rate of CIPS/CN (451.0 μmol h^{-1} g^{-1}) was 2.5 and 21.5 times higher than those of individual CIPS and CN, respectively, as exhibited in Fig. 12j. As the temperature increases, the difference of H_2 evolution rate between CIPS/CN and its components decreases (see Fig. 12k) due to the loss of ferroelectricity. Furthermore, the wavelength-dependent apparent quantum efficiency (AQE) for

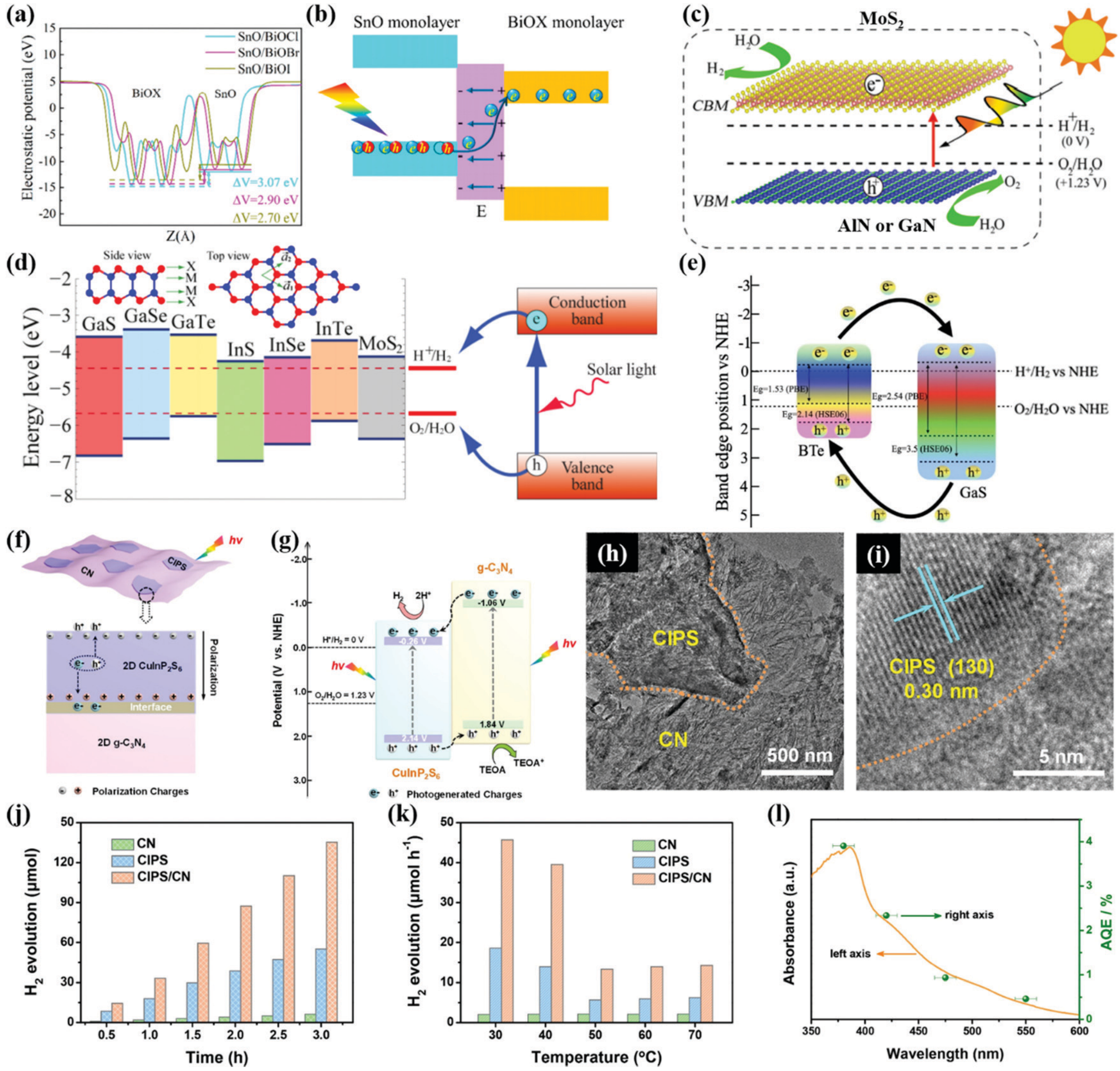

Fig. 12 (a) Calculated electrostatic potential and (b) the diagrammatic view illustrating the photoexcitation process under a built-in electric field of the SnO/BiOX bilayer. Reprinted with permission.[241] Copyright 2020, American Chemical Society. (c) Schematic illustration for MoS_2/AlN(GaN) vdW heterostructures. Reproduced with permission.[245] Copyright 2014, American Chemical Society. (d) Band edge positions of single-layer MX relative to the vacuum level at zero strain calculated with the HSE06 functional. The band edge positions of single-layer MoS_2 and the standard redox potentials for water splitting at pH 0 are shown for comparison. Reprinted with permission.[49] Copyright 2013, American Chemical Society. (e) Heterojunction charge transfer mechanism of the GaS/BTe vdW heterostructure. Reprinted with permission.[246] Copyright 2021, Elsevier. Schematic illustration of the transfer of photogenerated charges in (f) the interior of 2D ferroelectric $CuInP_2S_6$ and (g) the 2D/2D $CuInP_2S_6$/CN heterojunction system for photocatalytic H_2 evolution, (h and i) TEM images of CIPS/CN, (j) time-dependent photocatalytic H_2 evolution and (k) temperature-dependent photocatalytic H_2 evolution rates of different samples under visible-light irradiation (λ > 420 nm). (l) Wavelength-dependent AQE for photocatalytic H_2 evolution over CIPS/CN. Reprinted with permission.[248] Copyright 2020, Elsevier.

H_2 evolution over CIPS/CN as shown in Fig. 12l can reach 2.35% at 420 nm, surpassing those of many CN heterojunctions. Apparently, the ferroelectric effect of CIPS plays an important role in the photocatalytic H_2 evolution.

Based on the above, 2D materials can form various heterostructures, which greatly facilitate the photocatalytic reactions for water splitting. Thanks to the tunable electronic structures of 2D materials, different types of heterojunctions can be constructed based on the same materials. For instance, layered BP and CN often form a nested type I structure owing to their band structures.[249] However, BP quantum dots (BPQDs) exhibit a CBM higher than that of CN due to the quantum confinement effect.[250] Thus, the BPQDs form a type-II heterostructure with CN. In the heterostructure of BP and Bi_2WO_6, the electrons in the CB of Bi_2WO_6 combine with the holes in the VB of BP, forming a Z-scheme heterojunction. However, the n-type Bi_2WO_6 shows a lower Fermi level near its CB, while BP shows a higher Fermi level near its VB. Once these two E_F levels reach the equilibrium level, an IEF is formed and the Z-scheme is converted to the S-scheme.[251] The photocatalytic H_2 production activity of various 2D material based heterostructures is summarized in Table 1.

Table 1 Summary of vdW heterostructures for photocatalytic/photoelectrochemical H_2 production under solar light or visible light ($\lambda > 400$ nm)

Photocatalysts	Morphology	Heterojunction type	Light source and intensity	Electrolyte or scavenger	Published year	H_2 evolution rate	Ref.
BP/CN	2D/2D	Type-I	Xe lamp ($\lambda \geq 420$ nm)/300 mW cm^{-2}	Methanol	2017	1.3 mmol h^{-1} g^{-1}	100
BP/CdS	2D/0D	Type-II	Xe lamp ($\lambda \geq 420$ nm)/80 mW cm^{-2}	Lactic acid	2017	11.2 mmol h^{-1} g^{-1}	111
BPQDs/CN	0D/2D	Type-II	$\lambda \geq 420$ nm	Methanol	2018	271.0 μmol h^{-1} g^{-1}	250
BP/BiVO$_4$	2D/1.5D	Z-scheme	Xe lamp ($\lambda \geq 420$ nm)/400 mW cm^{-2}	Ethylenediaminetetraacetic acid (EDTA)	2018	160.0 μmol h^{-1} g^{-1}	29
BP/Au/CdS	2D/3D	Schottky junction	Xe lamp (full solar spectrum)/300 mW cm^{-2}	Na$_2$SO$_3$/Na$_2$S	2018	8.6 mmol h^{-1} g^{-1}	97
BP/CoP	0D/2D	-	Xe lamp ($\lambda \geq 420$ nm)	Oxalic acid	2018	694 μmol h^{-1} g^{-1}	252
BP/TiO$_2$	2D/3D	Z-scheme	Sunlight lamp/100 mW cm^{-2}	Chloroplatinic acid	2018	2.0 mmol h^{-1} g^{-1}	87
BP-MoS$_2$/CdS	3D/2D/2D	—	Solar simulator/100 mW cm^{-2}	Lactic acid	2019	183.2 mmol h^{-1} g^{-1}	98
MoS$_2$-BP/GO	2D/2D/3D	—	Xe lamp ($\lambda \geq 420$ nm)	Methanol	2019	8.7 mmol h^{-1} g^{-1}	253
BP/Bi$_2$WO$_6$	2D/2D	Z-scheme	Xe lamp ($\lambda \geq 420$ nm)	TEOA	2019	4.2 mmol h^{-1} g^{-1}	115
BP/CN	2D/2D	Type-I	Xe lamp ($\lambda \geq 420$ nm)	TEOA	2019	384.2 μmol h^{-1} g^{-1}	102
BP/Co$_2$P	2D/3D	-	Xe lamp ($\lambda \geq 420$ nm)	Na$_2$SO$_3$/Na$_2$S	2019	1.2 mmol h^{-1} g^{-1}	254
BP/RP	2D/2D	Z-scheme	LED light source ($\lambda \geq 420$ nm)	Pure water	2019	3.0 mmol h^{-1} g^{-1}	255
BP/MoS$_2$	2D/2D	Type-II	Xe lamp ($\lambda \geq 420$ nm)/150 mW cm^{-2}	Na$_2$SO$_3$/Na$_2$S	2021	575.4 μmol h^{-1} g^{-1}	256
CN/CoTiO$_3$	2D/3D	Z-scheme	Xe lamp (simulated solar light)/190 mW cm^{-2}	Ethanol solution	2016	858.0 μmol h^{-1} g^{-1}	149
Ni(OH)$_2$-CdS/CN	Core–shell	—	Xe lamp ($\lambda \geq 420$ nm)	Na$_2$SO$_3$/Na$_2$S	2016	115.2 mmol h^{-1} g^{-1}	257
CN/MoS$_2$/TiO$_2$	2D/3D	—	300W Xe arc lamp ($\lambda \geq 400$ nm)	Methanol	2016	1.3 mmol h^{-1} g^{-1}	258
CN/CuS/CdS	2D/3D	p–n junctions	Xe arc lamp ($\lambda \geq 400$ nm)/70 mW cm^{-2}	Na$_2$SO$_3$/Na$_2$S	2017	1.2 mmol h^{-1} g^{-1}	259
CN/Ni$_2$P-Cd$_{0.9}$Zn$_{0.1}$S	2D/1D	Type-II	Xe lamp ($\lambda \geq 420$ nm)	TEOA	2017	2.1 mmol h^{-1} g^{-1}	140
CN/PSi	2D/3D	Z-scheme	Xe lamp ($\lambda \geq 400$ nm) 100 mW cm^{-2}	TEOA	2017	870.4 μmol h^{-1} g^{-1}	260
CN/rGO	2D/2D	-	Xe lamp ($\lambda > 420$ nm)	TEOA	2018	715.0 μmol h^{-1} g^{-1}	261
CN/Ni$_2$P/ZrO$_2$	2D/3D	Type-II	Xe lamp ($\lambda \geq 420$ nm)	TEOA	2018	10.0 mmol h^{-1} g^{-1}	262
CN/phosphorene	2D/2D	Type-I	Xe lamp ($\lambda \geq 400$ nm)	Lactic acid	2018	571.0 μmol h^{-1} g^{-1}	101
CN/TiO$_2$/Ni$_x$P	2D/3D	Type-II	Xe lamp ($\lambda \geq 420$ nm)/57.1 mW cm^{-2}	TEOA	2018	5.4 mmol h^{-1} g^{-1}	263
CN/WO$_3$	2D/1.5D	S-scheme	Xe lamp (full solar spectrum)	Lactic acid	2019	982.0 μmol h^{-1} g^{-1}	153
CN/MoS$_2$	2D/2D	Type-I	Xe lamp ($\lambda \geq 420$ nm)	TEOA	2019	1.2 mmol h^{-1} g^{-1}	120
CN/S-PAN-2	2D/3D	—	Xe lamp ($\lambda \geq 420$ nm)	TEOA	2019	764.2 μmol h^{-1} g^{-1}	264
CN/CdS	2D/3D	Type-II	Xe arc lamp ($\lambda \geq 400$ nm)	TEOA	2019	5.4 mmol h^{-1} g^{-1}	265
CN/Zn$_x$Cd$_{1-x}$In$_2$S$_4$	2D/2D	Type-II	Xe lamp ($\lambda \geq 420$ nm)	TEOA	2019	170.3 μmol h^{-1} g^{-1}	266
RP/CN	2D/2D	Type-II	Xe lamp (full arc irradiation)	Pure water	2020	367.0 μmol h^{-1} g^{-1}	267
NiCoP/CN	3D/2D	—	Xe lamp ($\lambda \geq 420$ nm)	TEOA	2020	1.4 mmol h^{-1} g^{-1}	268
CN/carbon dots/CoO	2D/0D	Type-II	Xe lamp ($\lambda \geq 420$ nm)	TEOA	2020	987.4 μmol h^{-1} g^{-1}	269
CN/SiOC	2D/3D	Type-II	Xe lamp (simulated sunlight)	TEOA	2020	1.0 mmol h^{-1} g^{-1}	270
CN/CoFe$_2$O$_4$	2D/3D	Type-II	Direct sunlight	Methanol	2020	2.7 mmol h^{-1} g^{-1}	271
CN/Mn$_{0.5}$Cd$_{0.5}$Se	2D/3D	S-scheme	Xe lamp (full solar spectrum)	Na$_2$SO$_3$/Na$_2$S	2021	5.9 mmol h^{-1} g^{-1}	272
CN/SnO$_2$	2D/0D	Type-II	Xe lamp ($\lambda \geq 400$ nm)	TEOA	2021	2.5 mmol h^{-1} g^{-1}	273
CN/Cd$_{4-x}$Zn$_x$In$_{16}$S$_{35}$	2D/0D	Z-scheme	Xe lamp (full solar spectrum)	TEOA	2021	288.0 μmol h^{-1} g^{-1}	274
CN/LaFeO$_3$	2D/0D	Z-scheme	Xe lamp ($\lambda \geq 420$ nm)/100 mW cm^{-2}	TEOA	2021	1.3 mmol h^{-1} g^{-1}	275
MoS$_2$/TiO$_2$	2D/1D	—	Xe lamp (full solar spectrum)	Ethanol	2016	4.3 mmol h^{-1} g^{-1}	276
MoS$_2$/CdS	2D/1D	—	Xe lamp ($\lambda \geq 420$ nm)/100 mW cm^{-2}	Lactic acid	2016	49.8 mmol h^{-1} g^{-1}	277
MoS$_2$/CuInS$_2$	2D/3D	—	Xe lamp ($\lambda > 420$ nm)	Na$_2$SO$_3$/Na$_2$S	2016	316.0 μmol h^{-1} g^{-1}	278
WS$_2$/CdS	2D/1D	—	Xe arc lamp ($\lambda > 420$ nm)	Na$_2$SO$_3$/Na$_2$S	2016	1.8 mmol h^{-1} g^{-1}	279
WS$_2$/CdS	2D/1D	—	Arc lamp ($\lambda \geq 400$ nm)	Lactic acid	2016	1.2 mmol h^{-1} g^{-1}	280
MoS$_2$/CdS	2D/1D	—	Xe lamp ($\lambda > 400$ nm)	Lactic acid	2016	17.5 mmol h^{-1} g^{-1}	281
MoS$_2$/Mo/CdS	2D/3D	—	Xe lamp ($\lambda \geq 420$ nm)/52.2 mW cm^{-2}	Na$_2$SO$_3$/Na$_2$S	2017	4.5 mmol h^{-1} g^{-1}	282
MoS$_2$/rGO/CdS	2D/3D	—	Xe lamp ($\lambda \geq 400$ nm)/100 mW cm^{-2}	Lactic acid	2017	5.3 mmol h^{-1} g^{-1}	283
WS$_2$-MoS$_2$/CdS	2D/1D	—	AM 1.5G solar simulator/100 mW cm^{-2}	Lactic acid	2017	209.8 mmol h^{-1} g^{-1}	284
MoS$_2$/CdS	2D/1D	—	Xe lamp ($\lambda > 420$ nm)/160 mW cm^{-2}	Na$_2$SO$_3$/Na$_2$S	2017	9.7 mmol h^{-1} g^{-1}	285
BiOI-MoS$_2$/CdS	2D/3D	—	Xe lamp ($\lambda > 420$ nm)	Lactic acid	2017	9.7 mmol h^{-1} g^{-1}	286
MoS$_2$/AgInZnS	2D/3D	—	Xe lamp ($\lambda \geq 420$ nm)	Lactic acid	2017	19.9 mmol h^{-1} g^{-1}	287
MoSe$_2$/MoS$_2$	2D/2D	—	Xe lamp ($\lambda > 420$ nm)	TEOA	2017	4.6 mmol h^{-1} g^{-1}	288
MoS$_2$-CdS/RGO	2D/3D	—	Xe arc lamp ($\lambda \geq 420$ nm)/100 mW cm^{-2}	Lactic acid	2018	36.7 mmol h^{-1} g^{-1}	289
MoS$_2$/CdS	Core–shell	—	Xe lamp ($\lambda > 420$ nm)	Lactic acid	2018	1.4 mmol h^{-1} g^{-1}	290
MoS$_2$/ZnIn$_2$S$_4$	2D/3D	Type-I	Xe lamp ($\lambda > 420$ nm)	Na$_2$SO$_3$/Na$_2$S	2018	3.9 mmol h^{-1} g^{-1}	291
WS$_2$/CN/CdS	2D/3D	Type-II	Xe lamp ($\lambda > 420$ nm)	TEOA	2018	1.2 mmol h^{-1} g^{-1}	292
WS$_2$/CdS	2D/3D	—	Xe lamp ($\lambda > 400$ nm)	Lactic acid	2018	14.1 mmol h^{-1} g^{-1}	293
WS$_2$/ZnIn$_2$S$_4$	2D/3D	—	Xe lamp ($\lambda \geq 420$ nm)/15 mW cm^{-2}	Na$_2$SO$_3$/Na$_2$S	2018	199.1 μmol h^{-1} g^{-1}	294

Table 1 (*continued*)

Photocatalysts	Morphology	Heterojunction type	Light source and intensity	Electrolyte or scavenger	Published year	H_2 evolution rate	Ref.
MoS_2/$Mn_{0.2}Cd_{0.8}S$/MnS	2D/3D	Type-II	Xe lamp ($\lambda \geq 420$ nm)	Na_2SO_3/Na_2S	2019	19.9 mmol h^{-1} g^{-1}	295
MoS_2/PyP	2D/3D	Type-II	Xe lamp ($\lambda \geq 420$ nm)	Methanol	2019	540 μmol h^{-1} g^{-1}	296
MoS_2/CdS	2D/1D	—	Xe lamp ($\lambda \geq 420$ nm)	Lactic acid	2019	3.1 mmol h^{-1} g^{-1}	297
Au-MoS_2/$ZnIn_2S_4$	2D/3D	P–N heterojunction	Xe arc lamp ($\lambda > 400$ nm)	Na_2SO_3/Na_2S	2019	2.8 mmol h^{-1} g^{-1}	298
MoS_2/ZnO	2D/1D	—	Natural solar light	Na_2SO_4/Na_2S	2019	17.3 mmol h^{-1} g^{-1}	299
In_2S_3-MoS_2/MnS	2D/1D	—	Xe lamp ($\lambda > 400$ nm)	Na_2SO_3/Na_2S	2019	49.6 mmol h^{-1} g^{-1}	300
MoS_2/$SnNb_2O_6$	2D/2D	—	Xe lamp ($\lambda \geq 420$ nm)/180 mW cm^{-2}	Methanol	2019	322.5 μmol h^{-1} g^{-1}	301
MoS_2/$Mn_{0.2}Cd_{0.8}S$/Co_3O_4	2D/3D	Type-II	Xe lamp ($\lambda \geq 420$ nm)	Na_2SO_3/Na_2S	2020	16.5 mmol h^{-1} g^{-1}	302
MoS_2/$Mn_{0.2}Cd_{0.8}S$	2D/3D	—	Xe lamp ($\lambda \geq 420$ nm)	Na_2SO_3/Na_2S	2020	2 mmol h^{-1} g^{-1}	303
MoS_2/$LiNb_3O_8$	2D/1D	—	Hg lamp (185–500 nm)	Na_2SO_3/Na_2S	2020	900.0 μmol h^{-1} g^{-1}	304
MoS_2/Ti_3C_2	2D/2D	—	Xe lamp ($\lambda > 400$ nm)	Methanol	2020	6.1 mmol h^{-1} g^{-1}	228
WS_2/WO_3/CdS/	2D/0D	Z-scheme	Xe lamp ($\lambda > 420$ nm)	Lactic acid	2020	14.3 mmol h^{-1} g^{-1}	189
WS_2/$ZnIn_2S_4$	2D/2D	—	Xe lamp ($\lambda \geq 420$ nm)	Lactic acid	2020	2.6 mmol h^{-1} g^{-1}	305
WS_2/WO_3	2D/1.5D	Z-scheme	Xe lamp (full solar spectrum)	Lactic acid	2020	680.0 μmol h^{-1} g^{-1}	306
WS_2/CdS	2D/1D	Type-I	Xe arc lamp ($\lambda > 395$ nm)	Lactic acid	2020	19.2 mmol h^{-1} g^{-1}	307
MoS_2/CdS	2D/1D	Type-I	Xe arc lamp ($\lambda > 395$ nm)	Lactic acid	2020	9.7 mmol h^{-1} g^{-1}	307
MoS_2/Ag–$AgVO_3$	2D/3D	Z-scheme	250W Xe-arc lamp ($\lambda > 420$ nm)	25 vol% methanol	2020	19.3 mmol h^{-1} g^{-1}	308
N-MoS_2/MoO_3	2D/3D	Z-scheme	400 W Xenon lamp ($\lambda > 420$ nm)	—	2021	118 μ mol $h^{-1}g^{-1}$	309
P-MoS_2/WO_3	2D/3D	Z-scheme	300 W simulated solar light source	Na_2SO_3/Na_2S	2021	73.8 μ mol $h^{-1}g^{-1}$	310
MoS_2/$MAPbI_3$	2D/3D	Type-II	Xe lamp ($\lambda \geq 420$ nm)	Ethyl acetate	2021	30.0 mmol h^{-1} g^{-1}	311
MoS_2/CdS	2D/3D	—	Xe lamp ($\lambda > 420$ nm)	Na_2SO_3/Na_2S	2021	34.1 mmol h^{-1} g^{-1}	312
WS_2-WO_3·H_2O/CN	2D/3D	Z-scheme	Xe lamp ($\lambda \geq 420$ nm)	Lactic acid	2021	1.3 mmol h^{-1} g^{-1}	313
MoS_2/CdS	2D/3D	—	Xe lamp ($\lambda \geq 420$ nm)	Lactic acid	2021	54.1 mmol h^{-1} g^{-1}	314
WS_2/MoS_2	2D/2D	Type-II	Xe lamp (full solar spectrum)	Ethanol	2021	9.8 mmol h^{-1} g^{-1}	190
MgAl-LDH/CeO_2	2D/3D	—	Hg lamp ($\lambda \geq 420$ nm)	Methanol	2016	16.5 mmol h^{-1} g^{-1}	315
ZnCr-LDH/CN	2D/2D	Type-II	Xe lamp ($\lambda \geq 420$ nm)	TEOA	2017	680.0 μmol h^{-1} g^{-1}	316
NiFe-LDH/rGO/$La_2Ti_2O_7$	2D/2D	—	AM 1.5/100 mW cm^{-2}	TEOA	2018	532.2 μmol h^{-1} g^{-1}	317
NiFe-LDH/CdS	2D/3D	—	Simulated solar light	Methanol	2018	469.0 μmol h^{-1} g^{-1}	199
ZnCr-LDH/$Co(OH)_2$	2D/2D	P–N heterojunction	Hg lamp ($\lambda > 400$ nm)	Methanol	2018	1.1 mmol h^{-1} g^{-1}	219
MgCr-LDH/MgO/$MgCr_2O_4$	2D/3D	—	Hg lamp ($\lambda > 400$ nm)/100 mW cm^{-2}	Methanol	2018	420.0 μmol h^{-1} g^{-1}	318
NiFe-LDH/MoS_2	2D/2D	Z-scheme	Hg lamp ($\lambda > 400$ nm)/100 mW cm^{-2}	Methanol	2019	18.4 mmol h^{-1} g^{-1}	218
ZnTi-LDH/CN	2D/2D	—	AM1.5G	Methanol	2019	161.9 μmol h^{-1} g^{-1}	319
CoAl-LDH/CN	2D/2D	Type-II	Xe lamp ($\lambda \geq 420$ nm)	TEOA	2020	680.1 μmol h^{-1} g^{-1}	202
CoAl-LDH/$Zn_xCd_{1-x}S$	2D/2D	—	LED white light (full solar spectrum)	Lactic acid	2020	30.3 mmol h^{-1} g^{-1}	320
NiAl-LDH/CN	2D/2D	—	Quartz tungsten halogen lamp (simulated solar light)/300 mW cm^{-2}	TEOA	2020	3.2 mmol h^{-1} g^{-1}	321
NiFe-LDH/CN	2D/2D	Type-II	AM 1.5	TEOA	2021	3.1 mmol h^{-1} g^{-1}	322
NiFe-LDH/$Zn_{0.5}Cd_{0.5}S$	2D/3D	—	Xe lamp ($\lambda \geq 420$ nm)	Lactic acid	2021	1.0 mmol h^{-1} g^{-1}	323
NiCo-LDH/NiCoP/Cu_3P	2D/3D	P-N heterojunction	$\lambda > 420$ nm	TEOA	2021	8.9 mmol h^{-1} g^{-1}	216
NiCo-LDH/CoO	2D/1D	Type-II	AM 1.5/100 mW cm^{-2}	Na_2SO_3/Na_2S	2021	1.5 mmol h^{-1} g^{-1}	203
NFe-LDH/$ZnIn_2S_4$	2D/1D	Type-II	Xe lamp ($\lambda \geq 420$ nm)	TEOA	2021	2.0 mmol h^{-1} g^{-1}	324
NiCo-LDH/RP	2D/3D	S-scheme	Visible light	TEOA	2021	7.4 mmol h^{-1} g^{-1}	325
NiAl-LDH/NiP_2/Cu_3P	2D/3D	—	$\lambda \geq 420$ nm	TEOA	2021	6.8 mmol h^{-1} g^{-1}	326
$Ti_3C_2T_x$/TiO_2	2D/3D	Schottky junction	Hg lamp ($\lambda > 400$ nm)	Methanol	2016	17.8 μmol h^{-1} g^{-1}	231
Ti_3C_2 MXene/CN	2D/2D	—	Xe lamp (simulated solar light)	TEOA	2018	5.1 mmol h^{-1} g^{-1}	327
$Ti_3C_2T_x$/TiO_2/Cu_2O(001)	2D/3D	—	Xe lamp (simulated solar light)	Methanol	2019	1.5 mmol h^{-1} g^{-1}	328
	2D/3D		Xe lamp ($350 < \lambda < 780$ nm)	Na_2SO_3/Na_2S	2019	2.0 mmol h^{-1} g^{-1}	236

Table 1 (*continued*)

Photocatalysts	Morphology	Heterojunction type	Light source and intensity	Electrolyte or scavenger	Published year	H_2 evolution rate	Ref.
$Ti_3C_2T_x$ MXenes/UiO-66-NH_2		Schottky junction					
Ti_3C_2 MXene/MoS_2/TiO_2	2D/2D/1.5D	—	Xe lamp/AM1.5	Acetone	2019	5.1 mmol h^{-1} g^{-1}	329
Ti_3C_2 MXene/CdS	2D/1D	Schottky junction	Xe lamp ($\lambda \geq 420$ nm)	Lactic acid	2020	2.4 mmol h^{-1} g^{-1}	330
Ti_3C_2 MXene/TiO_2/$ZnIn_2S_4$	2D/2D	—	Xe lamp (full solar spectrum)	Na_2SO_3/Na_2S	2020	1.2 mmol h^{-1} g^{-1}	237
$Ti_3C_2T_x$ MXene/CdS	2D/1D	—	Xe lamp ($\lambda \geq 420$ nm)	Methanol	2020	15.4 mmol h^{-1} g^{-1}	232
$Ti_{3\text{-}x}C_2T_y$/CdS/Au	2D/3D	Schottky junction	LED lamp ($\lambda \geq 420$ nm)	Lactic acid	2021	5.4 mmol h^{-1} g^{-1}	234
$Ti_3C_2T_x$ MXene/CdS	2D/1.5D	Schottky junction	Xe lamp ($\lambda \geq 420$ nm)	Lactic acid	2021	3.2 mmol h^{-1} g^{-1}	230
BiOCl-PbS	2D/3D	Type-II	Xe lamp (full solar spectrum)	Na_2SO_3/Na_2S	2019	16.0 μmol h^{-1} g^{-1}	331
$CuInP_2S_6$/CN	2D/2D	Type-II	Xe lamp ($\lambda \geq 420$ nm)	TEOA	2020	451.0 μmol h^{-1} g^{-1}	248

4 Summary and prospects

In summary, the very recent efforts on the design and construction of various 2D material-based heterostructures, their photocatalytic performances for H_2 production under solar light and the action mechanisms of different heterojunctions are reviewed. The band alignments in different types of heterojunctions, especially type-II, Z-scheme and S-scheme, successfully promote visible light absorption and charges separation in the water splitting reaction. As illustrated in a large number of studies, 2D material-based heterostructures have excellent photocatalytic H_2 production rates owing to the heterojunction configuration and synergy of the components in the heterostructures.

However, challenges remain which hinder the practical application of 2D material-based photocatalytic systems for H_2 production from water splitting. (1) The structure and morphology of 2D hetero-materials usually have a significant effect on the photocatalytic performance.[26,332] Nevertheless, controllable, large-scale, economical and efficient synthesis approaches are still waiting to be developed. The band structure and surface states of 2D semiconductors can be modulated by metal or non-metal doping, optimizing the charge transfer route at the interface of the heterojunction.[333] The doping in 2D material based heterostructures with controllable dopant distribution and composition should be more explored for efficient photocatalyst design. (2) The aggregation of 2D photocatalyst particles in a liquid photocatalytic system will decrease the surface area and active sites of photocatalysts, resulting in weakened photocatalytic activity and stability.[39,40] Except for the self-assembly or *in situ* integration of 2D thin materials with substrates, other functional and effective optimization approaches should be investigated. (3) It is still difficult to track the migration behaviors of the electrons or holes and intermediates during photocatalytic reactions. The investigation of the main bottleneck in photocatalytic reactions by catching the intrinsic features and charge transport pathway will offer superior guidance for designing highly efficient 2D material-based heterojunctions.[334,335] Thus, more advanced *in situ* or time-resolved characterization techniques should be developed and employed in the research of photocatalytic reactions over 2D material based photocatalysts. (4) The theoretical calculation can help in deconstructing the electronic structure of 2D materials in more depth and predict the electronic properties of 2D material-based heterojunctions.[336–339] Thus, theoretical simulations should be more employed to understand the mechanism behind the chemical reactions and predict novel functional photocatalysts.

Overall, 2D material-based photocatalysts are highly promising in H_2 production from water splitting under solar light to solve the energy crisis and environmental issues. The architectures of 2D material-based heterostructures with fine-tuned compositions, structures and interfacial reactions sites greatly promote light harvesting, charge separation and transfer, and the resulting photocatalytic performances. To realize optimized 2D photocatalysts, the electronic structure, surface states, energy band alignments with other materials, *etc.*, should be comprehensively considered based on both in-depth experimental and theoretical research studies, in which more signs of progress are yet to come. Ideal 2D based photocatalysts consist of two semiconductors with sufficient oxidative and reductive band edges and couple with intercalated atoms and adjustors for directional charge flow. Among various 2D material based heterostructures, CN and TMD based heterostructures are the most promising photocatalysts owing to their advantages, including large-scale synthesis and high efficiency for photocatalytic water splitting. On the other hand, the application of BP for H_2 production from water splitting is also promising thanks to its thickness dependent band structure. However, the investigation on BP as a photocatalyst is still in its infancy with challenges to be overcome, such as the stability issue.

We believe that the present report will encourage the photocatalytic community to gain a depth understanding of the field and excel in the knowledge to develop resilient and sustainable 2D-material photocatalysts for future applications.

Conflicts of interest

There are no conflicts to declare.

Acknowledgements

This work was supported by the National Natural Science Foundation of China (Grant No. 12074265), the Shenzhen Science and Technology Project (Grant No. JCYJ20180507182246321, JCYJ20210324095611032), and the Natural Science Foundation of Guangdong Province.

References

1 T. H. Oh, M. Hasanuzzaman, J. Selvaraj, S. C. Teo and S. C. J. R. Chua, *Renewable Sustainable Energy Rev.*, 2018, **81**, 3021–3031.

2 N. A. Ludin, N. I. Mustafa, M. M. Hanafiah, M. A. Ibrahim, M. A. M. Teridi, S. Sepeai, A. Zaharim and K. J. R. Sopian, *Renewable Sustainable Energy Rev.*, 2018, **96**, 11–28.

3 E. Kabir, P. Kumar, S. Kumar, A. A. Adelodun and K.-H. J. R. Kim, *Renewable Sustainable Energy Rev.*, 2018, **82**, 894–900.

4 K. Khanafer and K. J. R. E. Vafai, *Renewable Energy*, 2018, **123**, 398–406.

5 A. Fujishima and K. J. n. Honda, *Nature*, 1972, **238**, 37–38.

6 A. Kudo and Y. J. C. S. R. Miseki, *Chem. Soc. Rev.*, 2009, **38**, 253–278.

7 X. Chen, C. Li, M. Grätzel, R. Kostecki and S. S. J. C. S. R. Mao, *Chem. Soc. Rev.*, 2012, **41**, 7909–7937.

8 T. Hisatomi, J. Kubota and K. J. C. S. R. Domen, *Chem. Soc. Rev.*, 2014, **43**, 7520–7535.

9 J. Ran, J. Zhang, J. Yu, M. Jaroniec and S. Z. J. C. S. R. Qiao, *Chem. Soc. Rev.*, 2014, **43**, 7787–7812.

10 K. J. J. o. P. Maeda, *J. Photochem. Photobiol. C: Photochem. Rev.*, 2011, **12**, 237–268.

11 S. Chen, T. Takata and K. J. N. R. M. Domen, *Nat. Rev. Mater.*, 2017, **2**, 1–17.

12 H. Wang, L. Zhang, Z. Chen, J. Hu, S. Li, Z. Wang, J. Liu and X. Wang, *Chem. Soc. Rev.*, 2014, **43**, 5234–5244.

13 X. Li, R. Shen, S. Ma, X. Chen and J. Xie, *Appl. Surf. Sci.*, 2018, **430**, 53–107.

14 K. S. Novoselov, A. K. Geim, S. V. Morozov, D. Jiang, Y. Zhang, S. V. Dubonos, I. V. Grigorieva and A. A. J. S. Firsov, *Science*, 2004, **306**, 666–669.

15 J. C. Garcia, D. B. De Lima, L. V. Assali and J. F. Justo, *J. Phys. Chem. C*, 2011, **115**, 13242–13246.

16 B. Luo, G. Liu and L. J. N. Wang, *Nanoscale*, 2016, **8**, 6904–6920.

17 A. Zhao, H. Li, X. Hu, C. Wang, H. Zhang, J. Lu, S. Ruan and Y.-J. Zeng, *J. Phys. D: Appl. Phys.*, 2020, **53**, 293002.

18 A. Zhao, L. Zhang, Y. Guo, H. Li, S. Ruan and Y.-J. Zeng, *2D Mater.*, 2021, **8**, 012004.

19 C. Tan, X. Cao, X.-J. Wu, Q. He, J. Yang, X. Zhang, J. Chen, W. Zhao, S. Han and G.-H. J. C. R. Nam, *Chem. Rev.*, 2017, **117**, 6225–6331.

20 D. Deng, K. Novoselov, Q. Fu, N. Zheng, Z. Tian and X. J. N. N. Bao, *Nat. Nanotechnol.*, 2016, **11**, 218.

21 M.-Y. Li, C.-H. Chen, Y. Shi and L.-J. J. M. T. Li, *Mater. Today*, 2016, **19**, 322–335.

22 X. Li, Y. Dai, M. Li, W. Wei and B. Huang, *J. Mater. Chem. A*, 2015, **3**, 24055–24063.

23 X. Lv, W. Wei, Q. Sun, F. Li, B. Huang and Y. J. A. C. B. E. Dai, *Appl. Catal., B*, 2017, **217**, 275–284.

24 Z. Guo, J. Zhou, L. Zhu and Z. J. J. o. M. C. A. Sun, *J. Mater. Chem. A*, 2016, **4**, 11446–11452.

25 J. Low, S. Cao, J. Yu and S. Wageh, *Chem. Commun.*, 2014, **50**, 10768–10777.

26 T. A. Shifa, F. Wang, Y. Liu and J. He, *Adv. Mater.*, 2019, **31**, 1804828.

27 B. Song and S. Jin, *Joule*, 2017, **1**, 220–221.

28 D. Voiry, J. Yang and M. Chhowalla, *Adv. Mater.*, 2016, **28**, 6197–6206.

29 M. Zhu, Z. Sun, M. Fujitsuka and T. Majima, *Angew. Chem., Int. Ed.*, 2018, **57**, 2160–2164.

30 J. Yan, P. Verma, Y. Kuwahara, K. Mori and H. Yamashita, *Small*, 2018, **2**, 1800212.

31 Z.-K. Shen, Y.-J. Yuan, L. Pei, Z.-T. Yu and Z. Zou, *Chem. Eng. J.*, 2020, **386**, 123997.

32 T. H. Lee, S. Y. Kim and H. W. Jang, *Nanomaterials*, 2016, **6**, 194.

33 A. Mishra, A. Mehta, S. Basu, N. P. Shetti, K. R. Reddy and T. M. Aminabhavi, *Carbon*, 2019, **149**, 693–721.

34 M. Ismael, *J. Alloys Compd.*, 2020, **846**, 156446.

35 M. Tekalgne, A. Hasani, Q. Van Le and S. Y. Kim, *Funct. Compos. Struct.*, 2019, **1**, 012001.

36 Q. Lu, Y. Yu, Q. Ma, B. Chen and H. Zhang, *Adv. Mater.*, 2016, **28**, 1917–1933.

37 V.-H. Nguyen, T. P. Nguyen, T.-H. Le, D.-V. N. Vo, D. L. Nguyen, Q. T. Trinh, I. T. Kim and Q. V. Le, *J. Chem. Technol. Biotechnol.*, 2020, **95**, 2597–2607.

38 K. Ren, K. Wang, Y. Cheng, W. Tang and G. Zhang, *Nano Futures*, 2020, **4**, 032006.

39 B. Luo, G. Liu and L. Wang, *Nanoscale*, 2016, **8**, 6904–6920.

40 P. Ganguly, M. Harb, Z. Cao, L. Cavallo, A. Breen, S. Dervin, D. D. Dionysiou and S. C. Pillai, *ACS Energy Lett.*, 2019, **4**, 1687–1709.

41 Q. Weng, X. Wang, X. Wang, Y. Bando and D. Golberg, *Chem. Soc. Rev.*, 2016, **45**, 3989–4012.

42 L. H. Li and Y. Chen, *Adv. Funct. Mater.*, 2016, **26**, 2594–2608.

43 J. Zhang, Y. Chen and X. Wang, *Energ. Environ. Sci.*, 2015, **8**, 3092–3108.

44 C. Zhi, Y. Bando, C. Tang, H. Kuwahara and D. Golberg, *Adv. Mater.*, 2009, **21**, 2889–2893.

45 Z. Jin, X. Jiang, Q. Zhang, S. Huang, L. Zhang, L. Huang, T. He, H. Zhang, T. Ohno, S. Ruan and Y.-J. Zeng, *Commun. Mater.*, 2020, **1**, 90.

46 D. Voiry, A. Mohite and M. Chhowalla, *Chem. Soc. Rev.*, 2015, **44**, 2702–2712.

47 W. Choi, N. Choudhary, G. H. Han, J. Park, D. Akinwande and Y. H. Lee, *Mater. Today*, 2017, **20**, 116–130.

48 S. Demirci, N. Avazlı, E. Durgun and S. Cahangirov, *Phys. Rev. B*, 2017, **95**, 115409.
49 H. L. Zhuang and R. G. Hennig, *Chem. Mater.*, 2013, **25**, 3232–3238.
50 P. Li and I. Appelbaum, *Phys. Rev. B*, 2015, **92**, 195129.
51 X. Long, Z. Wang, S. Xiao, Y. An and S. Yang, *Mater. Today*, 2016, **19**, 213–226.
52 L. Mohapatra and K. Parida, *J. Mater. Chem. A*, 2016, **4**, 10744–10766.
53 Y. Lee, J. H. Choi, H. J. Jeon, K. M. Choi, J. W. Lee and J. K. Kang, *Energ. Environ. Sci.*, 2011, **4**, 914–920.
54 Y. Zhang, L. Zhang, L. Hu, S. Huang, Z. Jin, M. Zhang, X. Huang, J. Lu, S. Ruan and Y.-J. Zeng, *Dalton Trans.*, 2019, **48**, 426–434.
55 L. Li, Y. Yu, G. J. Ye, Q. Ge, X. Ou, H. Wu, D. Feng, X. H. Chen and Y. Zhang, *Nat. Nanotechnol.*, 2014, **9**, 372.
56 H. Liu, Y. Du, Y. Deng and D. Y. Peide, *Chem. Soc. Rev.*, 2015, **44**, 2732–2743.
57 L. Hu, J. Yuan, Y. Ren, Y. Wang, J.-Q. Yang, Y. Zhou, Y.-J. Zeng, S.-T. Han and S. Ruan, *Adv. Mater.*, 2018, **30**, 1801232.
58 J. Ran, G. Gao, F.-T. Li, T.-Y. Ma, A. Du and S.-Z. Qiao, *Nat. Commun.*, 2017, **8**, 1–10.
59 Y. Li, X. Deng, J. Tian, Z. Liang and H. Cui, *Appl. Mater. Today*, 2018, **13**, 217–227.
60 P. Vogt, P. De Padova, C. Quaresima, J. Avila, E. Frantzeskakis, M. C. Asensio, A. Resta, B. Ealet and G. Le Lay, *Phys. Rev. Lett.*, 2012, **108**, 155501.
61 L. Tao, E. Cinquanta, D. Chiappe, C. Grazianetti, M. Fanciulli, M. Dubey, A. Molle and D. Akinwande, *Nat. Nanotechnol.*, 2015, **10**, 227–231.
62 Y. Peng, Y. Li, Y. Ban, H. Jin, W. Jiao, X. Liu and W. Yang, *Science*, 2014, **346**, 1356–1359.
63 M. G. Campbell, S. F. Liu, T. M. Swager and M. Dincă, *J. Am. Chem. Soc.*, 2015, **137**, 13780–13783.
64 K. Zhao, S. Liu, G. Ye, Q. Gan, Z. Zhou and Z. He, *J. Mater. Chem. A*, 2018, **6**, 2166–2175.
65 J. W. Colson and W. R. Dichtel, *Nat. Chem.*, 2013, **5**, 453.
66 L. Wang, Y. Zhang, L. Chen, H. Xu and Y. Xiong, *Adv. Mater.*, 2018, **30**, 1801955.
67 M. Zhang and X. Wang, *Energ. Environ. Sci.*, 2014, **7**, 1902–1906.
68 S. J. A. Moniz, S. A. Shevlin, D. J. Martin, Z.-X. Guo and J. Tang, *Energ. Environ. Sci.*, 2015, **8**, 731–759.
69 H. Uk Lee, S. C. Lee, J. Won, B.-C. Son, S. Choi, Y. Kim, S. Y. Park, H.-S. Kim, Y.-C. Lee and J. Lee, *Sci. Rep.*, 2015, **5**, 8691.
70 Y. Liu, R. Cheng, L. Liao, H. Zhou, J. Bai, G. Liu, L. Liu, Y. Huang and X. Duan, *Nat. Commun.*, 2011, **2**, 579.
71 C. R. Dean, A. F. Young, I. Meric, C. Lee, L. Wang, S. Sorgenfrei, K. Watanabe, T. Taniguchi, P. Kim, K. L. Shepard and J. Hone, *Nat. Nanotechnol.*, 2010, **5**, 722–726.
72 J. Zhang, H. Hong, J. Zhang, H. Fu, P. You, J. Lischner, K. Liu, E. Kaxiras and S. Meng, *Nano Lett.*, 2018, **18**, 6057–6063.
73 Z. Ji, H. Hong, J. Zhang, Q. Zhang, W. Huang, T. Cao, R. Qiao, C. Liu, J. Liang, C. Jin, L. Jiao, K. Shi, S. Meng and K. Liu, *ACS Nano*, 2017, **11**, 12020–12026.
74 X. Niu, Y. Li, Y. Zhang, Q. Zheng, J. Zhao and J. Wang, *J. Mater. Chem. C*, 2019, **7**, 1864–1870.
75 K. Ren, J. Yu and W. Tang, *J. Appl. Phys.*, 2019, **126**, 065701.
76 K. Ren, Y. Luo, J. Yu and W. Tang, *Chem. Phys.*, 2020, **528**, 110539.
77 Y. Liu, N. O. Weiss, X. Duan, H.-C. Cheng, Y. Huang and X. Duan, *Nat. Rev. Mater.*, 2016, **1**, 16042.
78 A. J. Bard, *J. Photochem.*, 1979, **10**, 59–75.
79 Y. Zou, J.-W. Shi, D. Ma, Z. Fan, L. Lu and C. Niu, *Chem. Eng. J.*, 2017, **322**, 435–444.
80 J.-W. Shi, Y. Zou, D. Ma, Z. Fan, L. Cheng, D. Sun, Z. Wang, C. Niu and L. Wang, *Nanoscale*, 2018, **10**, 9292–9303.
81 Y. Zou, J.-W. Shi, D. Ma, Z. Fan, C. Niu and L. Wang, *ChemCatChem*, 2017, **9**, 3752–3761.
82 H. Kato, Y. Sasaki, N. Shirakura and A. Kudo, *J. Mater. Chem. A*, 2013, **1**, 12327–12333.
83 H. Tada, T. Mitsui, T. Kiyonaga, T. Akita and K. Tanaka, *Nat. Mater.*, 2006, **5**, 782–786.
84 X.-L. Yin, J. Liu, W.-J. Jiang, X. Zhang, J.-S. Hu and L.-J. Wan, *Chem. Commun.*, 2015, **51**, 13842–13845.
85 K. Iwashina, A. Iwase, Y. H. Ng, R. Amal and A. Kudo, *J. Am. Chem. Soc.*, 2015, **137**, 604–607.
86 J. Yu, S. Wang, J. Low and W. Xiao, *Phys. Chem. Chem. Phys.*, 2013, **15**, 16883–16890.
87 J. Wu, S. Huang, Z. Jin, J. Chen, L. Hu, Y. Long, J. Lu, S. Ruan and Y.-J. Zeng, *J. Mater. Sci.*, 2018, **53**, 16557–16566.
88 Q. Xu, L. Zhang, B. Cheng, J. Fan and J. Yu, *Chem*, 2020, **6**, 1543–1559.
89 J. Mu, F. Teng, H. Miao, Y. Wang and X. Hu, *Appl. Surf. Sci.*, 2020, **501**, 143974.
90 Y. Ren, D. Zeng and W.-J. Ong, *Chinese J. Catal.*, 2019, **40**, 289–319.
91 F. Xia, H. Wang and Y. Jia, *Nat. Commun.*, 2014, **5**, 4458.
92 J. Kim, S. S. Baik, S. H. Ryu, Y. Sohn, S. Park, B.-G. Park, J. Denlinger, Y. Yi, H. J. Choi and K. S. J. S. Kim, *Science*, 2015, **349**, 723–726.
93 J. Qiao, X. Kong, Z.-X. Hu, F. Yang and W. Ji, *Nat. Commun.*, 2014, **5**, 4475.
94 P. Li, J. Lu, H. Cui, S. Ruan and Y.-J. Zeng, *Mater. Adv.*, 2021, **2**, 2483–2509.
95 Y. Xu, X. Wang, M. Jin, K. Kempa and L. Shui, *ChemElectroChem*, 2020, **7**, 96–104.
96 W. Gao, X. Bai, Y. Gao, J. Liu, H. He, Y. Yang, Q. Han, X. Wang, X. Wu, J. Wang, F. Fan, Y. Zhou, C. Li and Z. Zou, *Chem. Commun.*, 2020, **56**, 7777–7780.
97 X. Cai, L. Mao, S. Yang, K. Han and J. Zhang, *ACS Energy Lett.*, 2018, **3**, 932–939.
98 D. A. Reddy, E. H. Kim, M. Gopannagari, Y. Kim, D. P. Kumar and T. K. Kim, *Appl. Catal., B*, 2019, **241**, 491–498.
99 G. Wang, W. Zhao, M. Zhong, Y. Li, S. Xiao, S. Dang, C. Li, X. Long and W. Zhang, *J. Phys.: Condens. Matter*, 2019, **31**, 465002.
100 M. Zhu, S. Kim, L. Mao, M. Fujitsuka, J. Zhang, X. Wang and T. Majima, *J. Am. Chem. Soc.*, 2017, **139**, 13234–13242.
101 J. Ran, W. Guo, H. Wang, B. Zhu, J. Yu and S.-Z. Qiao, *Adv. Mater.*, 2018, **30**, 1800128.

102 Q. Zhang, S. Huang, J. Deng, D. T. Gangadharan, F. Yang, Z. Xu, G. Giorgi, M. Palummo, M. Chaker and D. Ma, *Adv. Funct. Mater.*, 2019, **29**, 1902486.

103 Y. Zheng, Y. Chen, B. Gao, B. Lin and X. J. A. F. M. Wang, *Adv. Funct. Mater.*, 2020, **30**, 2002021.

104 M. Zhu, S. Kim, L. Mao, M. Fujitsuka, J. Zhang, X. Wang and T. J. J. o. t. A. C. S. Majima, *J. Am. Chem. Soc.*, 2017, **139**, 13234–13242.

105 J. Ran, W. Guo, H. Wang, B. Zhu, J. Yu and S. Z. J. A. m. Qiao, *Adv. Mater.*, 2018, **30**, 1800128.

106 M. Wen, J. Wang, R. Tong, D. Liu, H. Huang, Y. Yu, Z.-K. Zhou, P. K. Chu and X.-F. Yu, *Adv. Sci.*, 2019, **6**, 1970007.

107 R. Boppella, W. Yang, J. Tan, H.-C. Kwon, J. Park and J. Moon, *Appl. Catal., B*, 2019, **242**, 422–430.

108 Y. Qu and X. J. C. S. R. Duan, *Chem. Soc. Rev.*, 2013, **42**, 2568–2580.

109 O. Elbanna, M. Zhu, M. Fujitsuka and T. Majima, *ACS Catal.*, 2019, **9**, 3618–3626.

110 Y. Chen, T. Shi, P. Liu, X. Ma, L. Shui, C. Shang, Z. Chen, X. Wang, K. Kempa and G. Zhou, *J. Mater. Chem. A*, 2018, **6**, 19167–19175.

111 J. Ran, B. Zhu and S.-Z. Qiao, *Angew. Chem., Int. Ed.*, 2017, **56**, 10373–10377.

112 S. Zhang, G. Cheng, L. Guo, N. Wang, B. Tan and S. J. A. C. Jin, *Angew. Chem.*, 2020, **132**, 6063–6070.

113 F. Liu, R. Shi, Z. Wang, Y. Weng, C. M. Che and Y. J. A. C. Chen, *Angew. Chem.*, 2019, **131**, 11917–11921.

114 X. Chen, J. S. Ponraj, D. Fan and H. Zhang, *Nanoscale*, 2020, **12**, 3513–3534.

115 J. Hu, D. Chen, Z. Mo, N. Li, Q. Xu, H. Li, J. He, H. Xu and J. Lu, *Angew. Chem., Int. Ed.*, 2019, **58**, 2073–2077.

116 X. Li, J. Xiong, X. Gao, J. Ma, Z. Chen, B. Kang, J. Liu, H. Li, Z. Feng and J. Huang, *J. Hazard. Mater.*, 2020, **387**, 121690.

117 P. Wang, Y. Liu, N. Jiang, R. Jing, S. Li, Q. Zhang, H. Liu, J. Xiu, Z. Li and Y. Liu, *J. Mol. Liq.*, 2021, **329**, 115540.

118 Z. Yang and J. Hao, *Small Methods*, 2018, **2**, 1700296.

119 Y. Cai, G. Zhang and Y.-W. Zhang, *Sci. Rep.*, 2014, **4**, 6677.

120 Y.-J. Yuan, Z. Shen, S. Wu, Y. Su, L. Pei, Z. Ji, M. Ding, W. Bai, Y. Chen, Z.-T. Yu and Z. Zou, *Appl. Catal., B*, 2019, **246**, 120–128.

121 H. Yu, H. Ma, X. Wu, X. Wang, J. Fan and J. Yu, *Sol. RRL*, 2021, **5**, 2000372.

122 S. Huang, H. Yi, L. Zhang, Z. Jin, Y. Long, Y. Zhang, Q. Liao, J. Na, H. Cui, S. Ruan, Y. Yamauchi, T. Wakihara, Y. V. Kaneti and Y.-J. Zeng, *J. Hazard. Mater.*, 2020, **393**, 122324.

123 X. Zhou, Y. Liu, Z. Jin, M. Huang, F. Zhou, J. Song, J. Qu, Y.-J. Zeng, P.-C. Qian and W.-Y. Wong, *Adv. Sci.*, 2021, **8**, 2170020.

124 J. Fu, J. Yu, C. Jiang and B. Cheng, *Adv. Energy Mater.*, 2018, **8**, 1701503.

125 J. Wen, J. Xie, X. Chen and X. Li, *Appl. Surf. Sci.*, 2017, **391**, 72–123.

126 Z. Jin, Q. Zhang, J. Chen, S. Huang, L. Hu, Y.-J. Zeng, H. Zhang, S. Ruan and T. Ohno, *Appl. Catal., B*, 2018, **234**, 198–205.

127 L. Zhang, Z. Jin, J. Huang, Y. Zhang, S. Huang, Z. Wang, Y.-J. Zeng, V. Malgras, S. Ruan and Y. Yamauchi, *ACS Appl. Energy Mater.*, 2021, **4**, 5677–5686.

128 S. Cao, J. Low, J. Yu and M. Jaroniec, *Adv. Mater.*, 2015, **27**, 2150–2176.

129 L. Zhang, Z. Jin, H. Lu, T. Lin, S. Ruan, X. S. Zhao and Y.-J. Zeng, *ACS Omega*, 2018, **3**, 15009–15017.

130 T. Giannakopoulou, I. Papailias, N. Todorova, N. Boukos, Y. Liu, J. Yu and C. Trapalis, *Chem. Eng. J.*, 2017, **310**, 571–580.

131 B. Tao and Z. Yan, *J. Colloid Interface Sci.*, 2016, **480**, 118–125.

132 Q. Fan, Y. Huang, C. Zhang, J. Liu, L. Piao, Y. Yu, S. Zuo and B. Li, *Catal. Today*, 2016, **264**, 250–256.

133 B. Xue, H.-Y. Jiang, T. Sun and F. Mao, *Catal. Lett.*, 2016, **146**, 2185–2192.

134 P. Qiu, J. Yao, H. Chen, F. Jiang and X. Xie, *J. Hazard. Mater.*, 2016, **317**, 158–168.

135 J. Di, J. Xia, S. Yin, H. Xu, L. Xu, Y. Xu, M. He and H. Li, *J. Mater. Chem. A*, 2014, **2**, 5340–5351.

136 H. Xu, J. Yan, Y. Xu, Y. Song, H. Li, J. Xia, C. Huang and H. Wan, *Appl. Catal., B*, 2013, **129**, 182–193.

137 Y. Jiang, P. Liu, Y. Chen, Z. Zhou, H. Yang, Y. Hong, F. Li, L. Ni, Y. Yan and D. H. Gregory, *Appl. Surf. Sci.*, 2017, **391**, 392–403.

138 B. Wang, J. Zhang and F. Huang, *Appl. Surf. Sci.*, 2017, **391**, 449–456.

139 I. Khan, N. Baig and A. Qurashi, *ACS Appl. Energy Mater.*, 2019, **2**, 607–615.

140 Z. Qin, F. Xue, Y. Chen, S. Shen and L. Guo, *Appl. Catal., B*, 2017, **217**, 551–559.

141 F. Yu, Z. Wang, S. Zhang, H. Ye, K. Kong, X. Gong, J. Hua and H. Tian, *Adv. Funct. Mater.*, 2018, **28**, 1804512.

142 Y. Gong, X. Quan, H. Yu, S. Chen and H. Zhao, *Appl. Catal., B*, 2018, **237**, 947–956.

143 C. Yang, Z. Xue, J. Qin, M. Sawangphruk, S. Rajendran, X. Zhang and R. Liu, *J. Phys. Chem. C*, 2019, **123**, 4795–4804.

144 K. He, J. Xie, X. Luo, J. Wen, S. Ma, X. Li, Y. Fang and X. Zhang, *Chinese J. Catal.*, 2017, **38**, 240–252.

145 S. Huang, Y. Long, S. Ruan and Y.-J. Zeng, *ACS Omega*, 2019, **4**, 15593–15599.

146 Y. Che, B. Lu, Q. Qi, H. Chang, J. Zhai, K. Wang and Z. Liu, *Sci. Rep.*, 2018, **8**, 16504.

147 J. Wang, G. Wang, X. Wang, Y. Wu, Y. Su and H. Tang, *Carbon*, 2019, **149**, 618–626.

148 Y. You, S. Wang, K. Xiao, T. Ma, Y. Zhang and H. Huang, *ACS Sustainable Chem. Eng.*, 2018, **6**, 16219–16227.

149 R. Ye, H. Fang, Y.-Z. Zheng, N. Li, Y. Wang and X. Tao, *ACS Appl. Mater. Interfaces*, 2016, **8**, 13879–13889.

150 X. Chen, T. Hu, J. Zhang, C. Yang, K. Dai and C. Pan, *J. Alloys Compd.*, 2021, **863**, 158068.

151 T. Yan, H. Liu and Z. Jin, *Energy Fuels*, 2021, **35**, 856–867.

152 B. Zhang, H. Shi, Y. Yan, C. Liu, X. Hu, E. Liu and J. Fan, *Colloids Surf., A*, 2021, **608**, 125598.

153 J. Fu, Q. Xu, J. Low, C. Jiang and J. Yu, *Appl. Catal., B*, 2019, **243**, 556–565.

154 X. Xu, J. Wang and Y. Shen, *Langmuir*, 2021, **37**, 7254–7263.

155 S. Cao and J. Yu, *J. Phys. Chem. Lett.*, 2014, **5**, 2101–2107.

156 Y. Chen, F. Su, H. Xie, R. Wang, C. Ding, J. Huang, Y. Xu and L. Ye, *Chem. Eng. J.*, 2021, **404**, 126498.

157 Y. Qin, J. Lu, F. Meng, X. Lin, Y. Feng, Y. Yan and M. Meng, *J. Colloid Interface Sci.*, 2021, **586**, 576–587.

158 R. Shen, K. He, A. Zhang, N. Li, Y. H. Ng, P. Zhang, J. Hu and X. Li, *Appl. Catal., B*, 2021, **291**, 120104.

159 X. Li, W. Bi, L. Zhang, S. Tao, W. Chu, Q. Zhang, Y. Luo, C. Wu and Y. Xie, *Adv. Mater.*, 2016, **28**, 2427–2431.

160 W. Wang, J. Fang and X. Huang, *Appl. Surf. Sci.*, 2020, **513**, 145830.

161 S. Wang, F. Wang, Z. Su, X. Wang, Y. Han, L. Zhang, J. Xiang, W. Du and N. Tang, *Catalysts*, 2019, **9**, 439.

162 J.-W. Shi, Y. Zou, L. Cheng, D. Ma, D. Sun, S. Mao, L. Sun, C. He and Z. Wang, *Chem. Eng. J.*, 2019, **378**, 122161.

163 Q. H. Wang, K. Kalantar-Zadeh, A. Kis, J. N. Coleman and M. S. Strano, *Nat. Nanotechnol.*, 2012, **7**, 699–712.

164 M. Chhowalla, H. S. Shin, G. Eda, L. J. Li, K. P. Loh and H. Zhang, *Nat. Chem.*, 2013, **5**, 263–275.

165 Y. Zhao, Y. Cai, L. Zhang, B. Li, G. Zhang and J. T. L. Thong, *Adv. Funct. Mater.*, 2020, **30**, 1903929.

166 C. Li, Q. Cao, F. Wang, Y. Xiao, Y. Li, J.-J. Delaunay and H. Zhu, *Chem. Soc. Rev.*, 2018, **47**, 4981–5037.

167 M.-H. Chiu, C. Zhang, H.-W. Shiu, C.-P. Chuu, C.-H. Chen, C.-Y. S. Chang, C.-H. Chen, M.-Y. Chou, C.-K. Shih and L.-J. Li, *Nat. Commun.*, 2015, **6**, 7666.

168 J. Zhou, J. Lin, X. Huang, Y. Zhou, Y. Chen, J. Xia, H. Wang, Y. Xie, H. Yu, J. Lei, D. Wu, F. Liu, Q. Fu, Q. Zeng, C.-H. Hsu, C. Yang, L. Lu, T. Yu, Z. Shen, H. Lin, B. I. Yakobson, Q. Liu, K. Suenaga, G. Liu and Z. Liu, *Nature*, 2018, **556**, 355–359.

169 K.-A. N. Duerloo, Y. Li and E. J. Reed, *Nat. Commun.*, 2014, **5**, 4214.

170 P. Cheng, K. Sun and Y. H. Hu, *Nano Lett.*, 2016, **16**, 572–576.

171 R. J. Toh, Z. Sofer, J. Luxa, D. Sedmidubský and M. J. C. C. Pumera, *Chem. Commun.*, 2017, **53**, 3054–3057.

172 Y. Xiao, M. Zhou, J. Liu, J. Xu and L. Fu, *Sci. China Mater.*, 2019, **62**, 759–775.

173 X. Xu, G. Zhou, X. Dong and J. Hu, *ACS Sustainable Chem. Eng.*, 2017, **5**, 3829–3836.

174 A. Di Bartolomeo, *Nanomaterials*, 2020, **10**, 579.

175 M. Wang, P. Ju, J. Li, Y. Zhao, X. Han and Z. Hao, *ACS Sustainable Chem. Eng.*, 2017, **5**, 7878–7886.

176 S. Wang, C. Ren, H. Tian, J. Yu and M. Sun, *Phys. Chem. Chem. Phys.*, 2018, **20**, 13394–13399.

177 Z. Zhang, Q. Qian, B. Li and K. J. Chen, *ACS Appl. Mater. Interfaces*, 2018, **10**, 17419–17426.

178 D. Lu, H. Wang, X. Zhao, K. K. Kondamareddy, J. Ding, C. Li and P. Fang, *ACS Sustainable Chem. Eng.*, 2017, **5**, 1436–1445.

179 A. H. Hendi, A. M. Osman, I. Khan, T. A. Saleh, T. A. Kandiel, T. F. Qahtan and M. K. Hossain, *ACS Omega*, 2020, **5**, 31644–31656.

180 P. C. Nagajyothi, K. C. Devarayapalli, J. Shim and S. V. Prabhakar Vattikuti, *Int. J. Hydrogen Energy*, 2020, **45**, 32756–32769.

181 J. Tao, X. Yu, Q. Liu, G. Liu and H. Tang, *J. Colloid Interface Sci.*, 2021, **585**, 470–479.

182 Y. Jia, Z. Wang, X.-Q. Qiao, L. Huang, S. Gan, D. Hou, J. Zhao, C. Sun and D.-S. Li, *Chem. Eng. J.*, 2021, **424**, 130368.

183 P. Raizada, T. H. C. Nguyen, S. Patial, P. Singh, A. Bajpai, V.-H. Nguyen, D. L. T. Nguyen, X. Cuong Nguyen, A. Aslam Parwaz Khan, S. Rangabhashiyam, S. Young Kim and Q. V. Le, *Fuel*, 2021, **303**, 121302.

184 Q. Luan, C.-L. Yang, M.-S. Wang and X.-G. Ma, *Chin. J. Phys.*, 2017, **55**, 1930–1937.

185 M. Thripuranthaka, R. V. Kashid, C. S. Rout and D. J. Late, *Appl. Phys. Lett.*, 2014, **104**, 081911.

186 S. Ma, L. Zeng, L. Tao, C. Y. Tang, H. Yuan, H. Long, P. K. Cheng, Y. Chai, C. Chen, K. H. Fung, X. Zhang, S. P. Lau and Y. H. Tsang, *Sci. Rep.*, 2017, **7**, 3125.

187 W.-Z. Xiao, L. Xu, Q.-Y. Rong, X.-Y. Dai, C.-P. Cheng and L.-L. Wang, *Appl. Surf. Sci.*, 2020, **504**, 144425.

188 Z. Thiehmed, A. Shakoor and T. Altahtamouni, *Catalysts*, 2021, **11**, 1283.

189 C. Xue, P. Zhang, G. Shao and G. Yang, *Chem. Eng. J.*, 2020, **398**, 125602.

190 G.-J. Lai, L.-M. Lyu, Y.-S. Huang, G.-C. Lee, M.-P. Lu, T.-P. Perng, M.-Y. Lu and L.-J. Chen, *Nano Energy*, 2021, **81**, 105608.

191 Y. Fan, J. Wang and M. Zhao, *Nanoscale*, 2019, **11**, 14836–14843.

192 H. U. Din, M. Idrees, G. Rehman, C. V. Nguyen, L.-Y. Gan, I. Ahmad, M. Maqbool and B. Amin, *Phys. Chem. Chem. Phys.*, 2018, **20**, 24168–24175.

193 F. Wang, T. A. Shifa, X. Zhan, Y. Huang, K. Liu, Z. Cheng, C. Jiang and J. He, *Nanoscale*, 2015, **7**, 19764–19788.

194 S. Altaf, A. Haider, S. Naz, A. Ul-Hamid, J. Haider, M. Imran, A. Shahzadi, M. Naz, H. Ajaz and M. Ikram, *Nanoscale Res. Lett.*, 2020, **15**, 144.

195 X. Peng, Y. Yan, X. Jin, C. Huang, W. Jin, B. Gao and P. K. Chu, *Nano Energy*, 2020, **78**, 105234.

196 P. J. Sideris, U. G. Nielsen, Z. Gan and C. P. Grey, *Science*, 2008, **321**, 113.

197 A. Razzaq, S. Ali, M. Asif and S.-I. In, *Catalysts*, 2020, **10**, 1185.

198 H. Boumeriame, E. S. Da Silva, A. S. Cherevan, T. Chafik, J. L. Faria and D. Eder, *J. Energy Chem.*, 2022, **64**, 406–431.

199 H. Zhou, Y. Song, Y. Liu, H. Li, W. Li and Z. Chang, *Int. J. Hydrogen Energy*, 2018, **43**, 14328–14336.

200 G. Zheng, C. Wu, J. Wang, S. Mo, Y. Wang, Z. Zou, B. Zhou and F. Long, *RSC Adv.*, 2019, **9**, 24280–24290.

201 S. Das, S. Patnaik and K. M. Parida, *Inorg. Chem. Front.*, 2019, **6**, 94–109.

202 J. Zhang, Q. Zhu, L. Wang, M. Nasir, S.-H. Cho and J. Zhang, *Int. J. Hydrogen Energy*, 2020, **45**, 21331–21340.

203 Y. Wang, S. Guo, X. Xin, Y. Zhang, B. Wang, S. Tang and X. Li, *Appl. Surf. Sci.*, 2021, **549**, 149108.

204 S. Mancipe, F. Tzompantzi and R. Gómez, *Appl. Clay Sci.*, 2017, **136**, 67–74.

205 S. Li, L. Wang, Y. Li, L. Zhang, A. Wang, N. Xiao, Y. Gao, N. Li, W. Song, L. Ge and J. Liu, *Appl. Catal., B*, 2019, **254**, 145–155.

206 D. Kandi, D. P. Sahoo, S. Martha and K. Parida, *Adv. Mater. Interfaces*, 2019, **6**, 1900370.

207 C. Wang, B. Ma, S. Xu, D. Li, S. He, Y. Zhao, J. Han, M. Wei, D. G. Evans and X. Duan, *Nano Energy*, 2017, **32**, 463–469.

208 C. Wang, B. Ma, X. Cao, S. He, J. Han, M. Wei, D. G. Evans and X. Duan, *J. Mater. Chem. A*, 2018, **6**, 7871–7876.

209 D. P. Sahoo, S. Patnaik and K. Parida, *ACS Omega*, 2019, **4**, 14721–14741.

210 S. Nayak and K. M. Parida, *Sci. Rep.*, 2019, **9**, 2458.

211 H. Gao, R. Cao, X. Xu, S. Zhang, H. Yongshun, H. Yang, X. Deng and J. Li, *Appl. Catal., B*, 2019, **245**, 399–409.

212 A. Kumar, G. Sharma, A. Kumari, C. Guo, M. Naushad, D.-V. N. Vo, J. Iqbal and F. J. Stadler, *Appl. Catal., B*, 2021, **284**, 119808.

213 S. Megala, P. Ravi, P. Maadeswaran, M. Navaneethan, M. Sathish and R. Ramesh, *Nanoscale Adv.*, 2021, **3**, 2075–2088.

214 K. Iqbal, A. Iqbal, A. M. Kirillov, C. Shan, W. Liu and Y. Tang, *J. Mater. Chem. A*, 2018, **6**, 4515–4524.

215 K. Hu, A. D. Blair, E. J. Piechota, P. A. Schauer, R. N. Sampaio, F. G. L. Parlane, G. J. Meyer and C. P. Berlinguette, *Nat. Chem.*, 2016, **8**, 853–859.

216 M. Yang, Y. Li, T. Yan and Z. Jin, *Nanoscale*, 2021, **13**, 13858–13872.

217 L. Sun, Y. Zhuang, Y. Yuan, W. Zhan, X.-J. Wang, X. Han and Y. Zhao, *Adv. Energy Mater.*, 2019, **9**, 1902839.

218 S. Nayak, G. Swain and K. Parida, *ACS Appl. Mater. Interfaces*, 2019, **11**, 20923–20942.

219 D. P. Sahoo, S. Nayak, K. H. Reddy, S. Martha and K. Parida, *Inorg. Chem.*, 2018, **57**, 3840–3854.

220 S. Wang, B. Y. Guan, X. Wang and X. W. D. Lou, *J. Am. Chem. Soc.*, 2018, **140**, 15145–15148.

221 G. Wang, Y. Li, L. Xu, Z. Jin and Y. Wang, *Renewable Energy*, 2020, **162**, 535–549.

222 J. K. Im, E. J. Sohn, S. Kim, M. Jang, A. Son, K.-D. Zoh and Y. Yoon, *Chemosphere*, 2021, **270**, 129478.

223 Q. Zhong, Y. Li and G. Zhang, *Chem. Eng. J.*, 2021, **409**, 128099.

224 V. Sharma, A. Kumar and V. Krishnan, *Handbook of Smart Photocatalytic Materials*, Elsevier, 2020, pp. 247–267.

225 W. Huang, L. Hu, Y. Tang, Z. Xie and H. Zhang, *Adv. Funct. Mater.*, 2020, **30**, 2005223.

226 N. M. Abbasi, Y. Xiao, L. Zhang, L. Peng, Y. Duo, L. Wang, P. Yin, Y. Ge, H. Zhu, B. Zhang, N. Xie, Y. Duan, B. Wang and H. Zhang, *J. Mater. Chem. C*, 2021, **9**, 8395–8465.

227 Y. Cao, Y. Fang, X. Lei, B. Tan, X. Hu, B. Liu and Q. Chen, *J. Hazard. Mater.*, 2020, **387**, 122021.

228 J. Zhang, C. Xing and F. Shi, *Int. J. Hydrogen Energy*, 2020, **45**, 6291–6301.

229 J. Zhou, D. Li, W. Zhao, B. Jing, Z. Ao and T. An, *ACS Appl. Mater. Interfaces*, 2021, **13**, 23843–23852.

230 M. Ding, R. Xiao, C. Zhao, D. Bukhvalov, Z. Chen, H. Xu, H. Tang, J. Xu and X. Yang, *Sol. RRL*, 2021, **5**, 2000414.

231 H. Wang, R. Peng, Z. D. Hood, M. Naguib, S. P. Adhikari and Z. Wu, *ChemSusChem*, 2016, **9**, 1490–1497.

232 J.-Y. Li, Y.-H. Li, F. Zhang, Z.-R. Tang and Y.-J. Xu, *Appl. Catal., B*, 2020, **269**, 118783.

233 M. Ding, R. Xiao, C. Zhao, D. Bukhvalov, Z. Chen, H. Xu, H. Tang, J. Xu and X. Yang, *Sol. RRL*, 2021, **5**, 2000414.

234 Z. Li, W. Huang, J. Liu, K. Lv and Q. Li, *ACS Catal.*, 2021, **11**, 8510–8520.

235 R. Chen, P. Wang, J. Chen, C. Wang and Y. Ao, *Appl. Surf. Sci.*, 2019, **473**, 11–19.

236 P. Tian, X. He, L. Zhao, W. Li, W. Fang, H. Chen, F. Zhang, Z. Huang and H. Wang, *Int. J. Hydrogen Energy*, 2019, **44**, 788–800.

237 K. Huang, C. Li and X. Meng, *J. Colloid Interface Sci.*, 2020, **580**, 669–680.

238 A. VahidMohammadi, J. Rosen and Y. Gogotsi, *Science*, 2021, **372**, eabf1581.

239 G.-J. Lee, Y.-C. Zheng and J. J. Wu, *Catal. Today*, 2018, **307**, 197–204.

240 J. Xiong, P. Song, J. Di and H. Li, *J. Mater. Chem. A*, 2020, **8**, 21434–21454.

241 Y. Liu, P. Lv, W. Zhou and J. Hong, *J. Phys. Chem. C*, 2020, **124**, 9696–9702.

242 T. Rao, H. Wang, Y.-J. Zeng, Z. Guo, H. Zhang and W. Liao, *Adv. Sci.*, 2021, **8**, 2002284.

243 Y. Cui, L. Peng, L. Sun, Q. Qian and Y. Huang, *J. Mater. Chem. A*, 2018, **6**, 22768–22777.

244 S. Huang, Z. Shuai and D. Wang, *J. Mater. Chem. A*, 2021, **9**, 2734–2741.

245 J. Liao, B. Sa, J. Zhou, R. Ahuja and Z. Sun, *J. Phys. Chem. C*, 2014, **118**, 17594–17599.

246 D. Singh, N. Khossossi, A. Ainane and R. Ahuja, *Catal. Today*, 2021, **370**, 14–25.

247 X. Wang, K. Du, Y. Y. Fredrik Liu, P. Hu, J. Zhang, Q. Zhang, M. H. S. Owen, X. Lu, C. K. Gan, P. Sengupta, C. Kloc and Q. Xiong, *2D Mater.*, 2016, **3**, 031009.

248 B. Lin, A. Chaturvedi, J. Di, L. You, C. Lai, R. Duan, J. Zhou, B. Xu, Z. Chen, P. Song, J. Peng, B. Ma, H. Liu, P. Meng, G. Yang, H. Zhang, Z. Liu and F. Liu, *Nano Energy*, 2020, **76**, 104972.

249 S. Li, Y. Zhang and H. Huang, *J. Energy Chem.*, 2022, **67**, 745–779.

250 W. Lei, Y. Mi, R. Feng, P. Liu, S. Hu, J. Yu, X. Liu, J. A. Rodriguez, J.-o. Wang, L. Zheng, K. Tang, S. Zhu, G. Liu and M. Liu, *Nano Energy*, 2018, **50**, 552–561.

251 C. Chen, J. Hu, X. Yang, T. Yang, J. Qu, C. Guo and C. M. Li, *ACS Appl. Mater. Interfaces*, 2021, **13**, 20162–20173.

252 Q. Liang, F. Shi, X. Xiao, X. Wu, K. Huang and S. Feng, *ChemCatChem*, 2018, **10**, 2179–2183.

253 M. Zhu, M. Fujitsuka, L. Zeng, M. Liu and T. Majima, *Appl. Catal., B*, 2019, **256**, 117864.

254 Y.-J. Yuan, Z.-K. Shen, S. Song, J. Guan, L. Bao, L. Pei, Y. Su, S. Wu, W. Bai, Z.-T. Yu, Z. Ji and Z. Zou, *ACS Catal.*, 2019, **9**, 7801–7807.

255 F. Liu, R. Shi, Z. Wang, Y. Weng, C.-M. Che and Y. Chen, *Angew. Chem.*, 2019, **58**, 11791–11795.

256 Y. Huang, H. Lu, B. Wang, W. He, H. Dong, L. Sui, Z. Gan, S. Ma, B. Pang, L. Dong and L. Yu, *Int. J. Hydrogen Energy*, 2021, **46**, 3530–3538.

257 Z. Yan, Z. Sun, X. Liu, H. Jia and P. Du, *Nanoscale*, 2016, **8**, 4748–4756.

258 X. Yang, H. Huang, M. Kubota, Z. He, N. Kobayashi, X. Zhou, B. Jin and J. Luo, *Mater. Res. Bull.*, 2016, **76**, 79–84.

259 F. Cheng, H. Yin and Q. Xiang, *Appl. Surf. Sci.*, 2017, **391**, 432–439.

260 Y. Shi, J. Chen, Z. Mao, B. D. Fahlman and D. Wang, *J. Catal.*, 2017, **356**, 22–31.

261 J. Wan, C. Pu, R. Wang, E. Liu, X. Du, X. Bai, J. Fan and X. Hu, *Int. J. Hydrogen Energy*, 2018, **43**, 7007–7019.

262 J. Xu, J. Gao, Y. Qi, C. Wang and L. Wang, *ChemCatChem*, 2018, **10**, 3327–3335.

263 M. Wu, J. Zhang, C. Liu, Y. Gong, R. Wang, B. He and H. Wang, *ChemCatChem*, 2018, **10**, 3069–3077.

264 H. Che, C. Liu, H. Dong, C. Li, X. Liu and G. Che, *Int. J. Hydrogen Energy*, 2019, **44**, 20029–20041.

265 Y. Wang, X. Zhang, Y. Liu, Y. Zhao, C. Xie, Y. Song and P. Yang, *Int. J. Hydrogen Energy*, 2019, **44**, 30151–30159.

266 Y. Zou, J.-W. Shi, L. Sun, D. Ma, S. Mao, Y. Lv and Y. Cheng, *Chem. Eng. J.*, 2019, **378**, 122192.

267 M. Wang, Z. Qin, Z. Diao, R. Li, J. Zhong, D. Ma and Y. Chen, *ACS Sustain. Chem. Eng.*, 2020, **8**, 13459–13466.

268 C. Li, H. Wu, Y. Du, S. Xi, H. Dong, S. Wang and Y. Wang, *ACS Sustain. Chem. Eng.*, 2020, **8**, 12934–12943.

269 W. Shi, J. Wang, S. Yang, X. Lin, F. Guo and J. Shi, *J. Chem. Technol. Biotechnol.*, 2020, **95**, 2129–2138.

270 J. Pan, W. Shen, Y. Zhang, H. Tang, H. Sun, W. Zhong and X. Yan, *Appl. Surf. Sci.*, 2020, **520**, 146335.

271 M. Lallimathi, P. Kalisamy, M. Suryamathi, T. Alshahrani, M. Shkir, M. Venkatachalam and B. Palanivel, *ChemistrySelect*, 2020, **5**, 10607–10617.

272 Y. Chen, Q. Wang, H. Huang, J. Kou, C. Lu and Z. Xu, *Int. J. Hydrogen Energy*, 2021, **46**, 32514–32522.

273 J. Yan, Z. Song, H. Li, H. Xu and L. Y. S. Lee, *Chem. Eng. J.*, 2021, **425**, 131512.

274 Z. Wu, X.-L. Wang, X. Wang, X. Xu, D.-S. Li and T. Wu, *Chem. Eng. J.*, 2021, **426**, 131216.

275 Z. Tian, X. Yang, Y. Chen, X. Wang, T. Jiao, W. Zhao, H. Huang and J. Hu, *J. Alloys Compd.*, 2021, 161850.

276 H. He, J. Lin, W. Fu, X. Wang, H. Wang, Q. Zeng, Q. Gu, Y. Li, C. Yan, B. K. Tay, C. Xue, X. Hu, S. T. Pantelides, W. Zhou and Z. Liu, *Adv. Energy Mater.*, 2016, **6**, 1600464.

277 X.-L. Yin, L.-L. Li, W.-J. Jiang, Y. Zhang, X. Zhang, L.-J. Wan and J.-S. Hu, *ACS Appl. Mater. Interfaces*, 2016, **8**, 15258–15266.

278 Y.-J. Yuan, D.-Q. Chen, Y.-W. Huang, Z.-T. Yu, J.-S. Zhong, T.-T. Chen, W.-G. Tu, Z.-J. Guan, D.-P. Cao and Z.-G. Zou, *ChemSusChem*, 2016, **9**, 1003–1009.

279 Q. Xiang, F. Cheng and D. Lang, *ChemSusChem*, 2016, **9**, 996–1002.

280 J. He, L. Chen, Z.-Q. Yi, C.-T. Au and S.-F. Yin, *Ind. Eng. Chem. Res.*, 2016, **55**, 8327–8333.

281 Q. Liu, Q. Shang, A. Khalil, Q. Fang, S. Chen, Q. He, T. Xiang, D. Liu, Q. Zhang, Y. Luo and L. Song, *ChemCatChem*, 2016, **8**, 2614–2619.

282 L. Zhao, J. Jia, Z. Yang, J. Yu, A. Wang, Y. Sang, W. Zhou and H. Liu, *Appl. Catal., B*, 2017, **210**, 290–296.

283 M. Ben Ali, W.-K. Jo, H. Elhouichet and R. Boukherroub, *Int. J. Hydrogen Energy*, 2017, **42**, 16449–16458.

284 D. A. Reddy, H. Park, R. Ma, D. P. Kumar, M. Lim and T. K. Kim, *ChemSusChem*, 2017, **10**, 1563–1570.

285 Y. Li, L. Wang, T. Cai, S. Zhang, Y. Liu, Y. Song, X. Dong and L. Hu, *Chem. Eng. J.*, 2017, **321**, 366–374.

286 C. Zhou, H. Yang, G. Wang, J. Chen, R. Wang and C. Jiang, *Int. J. Hydrogen Energy*, 2017, **42**, 28337–28348.

287 T. Huang, W. Chen, T.-Y. Liu, Q.-L. Hao and X.-H. Liu, *Int. J. Hydrogen Energy*, 2017, **42**, 12254–12261.

288 J. Chen, X.-J. Wu, Y. Gong, Y. Zhu, Z. Yang, B. Li, Q. Lu, Y. Yu, S. Han, Z. Zhang, Y. Zong, Y. Han, L. Gu and H. Zhang, *J. Am. Chem. Soc.*, 2017, **139**, 8653–8660.

289 X.-L. Yin, L.-L. Li, D.-C. Li and J.-M. Dou, *Int. J. Hydrogen Energy*, 2018, **43**, 20382–20391.

290 Y. Liu, H. Niu, W. Gu, X. Cai, B. Mao, D. Li and W. Shi, *Chem. Eng. J.*, 2018, **339**, 117–124.

291 Z. Zhang, L. Huang, J. Zhang, F. Wang, Y. Xie, X. Shang, Y. Gu, H. Zhao and X. Wang, *Appl. Catal., B*, 2018, **233**, 112–119.

292 Y. Zou, J.-W. Shi, D. Ma, Z. Fan, L. Cheng, D. Sun, Z. Wang and C. Niu, *ChemSusChem*, 2018, **11**, 1187–1197.

293 K. Zhang, M. Fujitsuka, Y. Du and T. Majima, *ACS Appl. Mater. Interfaces*, 2018, **10**, 20458–20466.

294 J. Zhou, D. Chen, L. Bai, L. Qin, X. Sun and Y. Huang, *Int. J. Hydrogen Energy*, 2018, **43**, 18261–18269.

295 J. Wang, J. Luo, D. Liu, S. Chen and T. Peng, *Appl. Catal., B*, 2019, **241**, 130–140.

296 S. Zang, G. Zhang, Z.-A. Lan, D. Zheng and X. Wang, *Appl. Catal., B*, 2019, **251**, 102–111.

297 Z.-W. Zhang, Q.-H. Li, X.-Q. Qiao, D. Hou and D.-S. Li, *Chinese J. Catal.*, 2019, **40**, 371–379.

298 G. Swain, S. Sultana and K. Parida, *Inorg. Chem.*, 2019, **58**, 9941–9955.

299 S. Kumar, A. Kumar, V. Navakoteswara Rao, A. Kumar, M. V. Shankar and V. Krishnan, *ACS Appl. Energy Mater.*, 2019, **2**, 5622–5634.

300 M. Dan, J. Xiang, F. Wu, S. Yu, Q. Cai, L. Ye, Y. Ye and Y. Zhou, *Appl. Catal., B*, 2019, **256**, 117870.

301 D. Jiang, B. Wen, Y. Zhang, Y. Jin, D. Li and M. Chen, *J. Colloid Interface Sci.*, 2019, **536**, 1–8.

302 H.-Q. Feng, Y. Xi, H.-Q. Xie, Y.-K. Li and Q.-Z. Huang, *Int. J. Hydrogen Energy*, 2020, **45**, 10764–10774.

303 X. Liu, X. Chen, L. Xu, B. Wu, X. Tu, X. Luo, F. Yang and J. Lin, *Int. J. Hydrogen Energy*, 2020, **45**, 26770–26784.

304 H. Zhai, J. Qi, Y. Tan, L. Yang, H. Li, Y. Kang, H. Liu, J. Shang and H. S. Park, *Appl. Mater. Today*, 2020, **18**, 100536.

305 M. Xiong, B. Chai, J. Yan, G. Fan and G. Song, *Appl. Surf. Sci.*, 2020, **514**, 145965.

306 S. Zhang, S. Chen, D. Liu, J. Zhang and T. Peng, *Appl. Surf. Sci.*, 2020, **529**, 147013.

307 B. Archana, N. Kottam, S. Nayak, K. B. Chandrasekhar and M. B. Sreedhara, *J. Phys. Chem. C*, 2020, **124**, 14485–14495.

308 S. Bera, S. Ghosh and R. N. Basu, *J. Alloys Compd.*, 2020, **830**, 154527.

309 N. R. Khalid, M. Rizwan Kamal, M. B. Tahir, M. Rafique, N. A. Niaz, Y. Ali, M. Alzaid, H. Alrobei and S. Muhammad, *Int. J. Hydrogen Energy*, 2021, **46**, 39822–39829.

310 X. Wei, X. Zhang, S. Ali, W. Han, D. He, J. Wang, S. Kong, Z. Feng, G. Zhang and J. Qi, *J. Alloys Compd.*, 2021, **872**, 159637.
311 W. Guan, Y. Li, Q. Zhong, H. Liu, J. Chen, H. Hu, K. Lv, J. Gong, Y. Xu, Z. Kang, M. Cao and Q. Zhang, *Nano Lett.*, 2021, **21**, 597–604.
312 J. Chen, X.-J. Wu, Q. Lu, M. Zhao, P.-F. Yin, Q. Ma, G.-H. Nam, B. Li, B. Chen and H. Zhang, *Small*, 2021, **17**, 2006135.
313 X. Wang, G. Hai, B. Li, Q. Luan, W. Dong and G. Wang, *Chem. Eng. J.*, 2021, **426**, 130822.
314 L. Su, L. Luo, J. Wang, T. Song, W. Tu and Z.-J. Wang, *Catal. Sci. Technol.*, 2021, **11**, 1292–1297.
315 S. Nayak and K. M. Parida, *Int. J. Hydrogen Energy*, 2016, **41**, 21166–21180.
316 B. Luo, R. Song and D. Jing, *Int. J. Hydrogen Energy*, 2017, **42**, 23427–23436.
317 R. Boppella, C. H. Choi, J. Moon and D. Ha Kim, *Appl. Catal., B*, 2018, **239**, 178–186.
318 S. Nayak, A. C. Pradhan and K. M. Parida, *Inorg. Chem.*, 2018, **57**, 8646–8661.
319 D. Sun, D. Chi, Z. Yang, Z. Xing, J. Yin, Z. Li, Q. Zhu and W. Zhou, *Int. J. Hydrogen Energy*, 2019, **44**, 16348–16358.
320 H. Li, X. Hao, Y. Liu, Y. Li and Z. Jin, *J. Colloid Interface Sci.*, 2020, **572**, 62–73.
321 S. Megala, M. Sathish, S. Harish, M. Navaneethan, S. Sohila, B. Liang and R. Ramesh, *Appl. Surf. Sci.*, 2020, **509**, 144656.
322 J. Yan, X. Zhang, W. Zheng and L. Y. S. Lee, *ACS Appl. Mater. Interfaces*, 2021, **13**, 24723–24733.
323 Y. Sun, X. Wang, Q. Fu and C. Pan, *ACS Appl. Mater. Interfaces*, 2021, **13**, 39331–39340.
324 S. Zhao, Q. Liang, W. Gao, M. Zhou, C. Yao, S. Xu and Z. Li, *Inorg. Chem.*, 2021, **60**, 9762–9772.
325 L. Hu, J. Xu, Y. Liu and S. Zhao, *New J. Chem.*, 2021, **45**, 17984–17995.
326 X. Yan and Z. Jin, *Chem. Eng. J.*, 2021, **420**, 127682.
327 X. An, W. Wang, J. Wang, H. Duan, J. Shi and X. Yu, *Phys. Chem. Chem. Phys.*, 2018, **20**, 11405–11411.
328 C. Peng, W. Xu, P. Wei, M. Liu, L. Guo, P. Wu, K. Zhang, Y. Cao, H. Wang, H. Yu, F. Peng and X. Yan, *Int. J. Hydrogen Energy*, 2019, **44**, 29975–29985.
329 Y. Li, Z. Yin, G. Ji, Z. Liang, Y. Xue, Y. Guo, J. Tian, X. Wang and H. Cui, *Appl. Catal., B*, 2019, **246**, 12–20.
330 R. Xiao, C. Zhao, Z. Zou, Z. Chen, L. Tian, H. Xu, H. Tang, Q. Liu, Z. Lin and X. Yang, *Appl. Catal., B*, 2020, **268**, 118382.
331 J. Lu, Y. Chen, L. Li, X. Cai, S. Zhong, L. Wu, J. Chen and S. Bai, *Chem. Eng. J.*, 2019, **362**, 1–11.
332 R. Hu, G. Liao, Z. Huang, H. Qiao, H. Liu, Y. Shu, B. Wang and X. Qi, *J. Hazard. Mater.*, 2021, **405**, 124179.
333 Y.-Y. Wang, Y.-X. Chen, T. Barakat, Y.-J. Zeng, J. Liu, S. Siffert and B.-L. Su, *J. Energy Chem.*, 2022, **66**, 529–559.
334 X. Liu, Q. Zhang and D. Ma, *Sol. RRL*, 2021, **5**, 2000397.
335 C.-F. Fu, J. Sun, Q. Luo, X. Li, W. Hu and J. Yang, *Nano Lett.*, 2018, **18**, 6312–6317.
336 C.-F. Fu, X. Wu and J. Yang, *Adv. Mater.*, 2018, **30**, 1802106.
337 A. K. Singh, K. Mathew, H. L. Zhuang and R. G. Hennig, *J. Phys. Chem. Lett.*, 2015, **6**, 1087–1098.
338 Y. Li, Y.-L. Li, B. Sa and R. Ahuja, *Catal. Sci. Technol.*, 2017, **7**, 545–559.
339 X. Zhang, Z. Zhang, D. Wu, X. Zhang, X. Zhao and Z. Zhou, *Small*, 2018, **2**, 1700359.